学位論文（要約）

Magnetism of buried layers studied by soft X-ray resonant magneto-optical effect using polarization modulation

（偏光変調型軟 X 線共鳴磁気光学効果による
埋込層の磁性研究）

平成 28 年 12 月　博士（理学）申請

東京大学大学院理学系研究科
物理学専攻

久保田　雄也

Magnetism of buried layers studied by soft X-ray resonant magneto-optical effect using polarization modulation

THE UNIVERSITY OF TOKYO

Yuya Kubota
Department of Physics, Graduate School of Science
The University of Tokyo

A thesis submitted for the degree of
Doctor of Philosophy
December, 2016

Supervisor: Professor Iwao Matsuda

Abstract

Magnetism has been attracting great interest in for many years because its research has led us deep understanding of our nature and the application has become highly necessary in our society. Experimentally, light or an electromagnetic wave has been used as a probe to investigate magnetic materials via the magneto-optical effects. Especially, since the novel spintronics materials, such as heterostructures of magnetic and topological insulators (TIs), are paid attention nowadays, the magneto-optical effect in the vacuum ultraviolet $\sim$ soft X-ray energy region is expected as a powerful method with element-selectivity and a resonant enhancement in order to understand their buried magnetism. However, only the magnetic circular dichroism (MCD) that is just one of the phenomena of the magneto-optical effect has been mostly discussed. It is required to develop new methods that enable us to obtain both of the magneto-optical parameters, MCD and the optical rotation, and to investigate magnetism using them.

In the present thesis, we studied the magnetism of buried layers using the magneto-optical effect in the soft X-ray energy region. We also developed a new method with a polarization modulated synchrotron radiation. The first issue is the origin of the proximity effect that induces a magnetic order in a TI at the interface with a magnetic material as one of the interesting magnetic phenomena at buried layers. By angle-resolved photoelectron spectroscopy (ARPES) and X-ray MCD (XMCD) measurements of the TI, Bi_2Se_3, on a ferrimagnetic insulator, $Y_3Fe_5O_{12}$ (YIG), the Dirac-like surface state of Bi_2Se_3 was directly observed and the localized $3d$ spin states of Fe^{3+} in YIG were confirmed. We also proposed the interface model that the proximity effect is likely described in terms of the exchange interaction between the localized Fe $3d$ electrons in YIG and the delocalized electrons of the surface and bulk states in Bi_2Se_3 observed by ARPES. However, because we only had indirect evidences of TI's magnetism at the buried interface, we have to focus on the bulk sensitive method with high accuracy, resonant magneto-optical Kerr effect (MOKE) measurement, to investigate buried magnetic layers. Therefore, second subject is the study of L-edge resonant MOKE of a buried Fe film to get a deeper understanding of resonant MOKE. The sign change of the Kerr rotation angle (θ_K) between the L_3- and L_2-edges was first observed in the experiment and reproduced by the classical electromagnetic simulation using empirical optical constants. In addition, the spectrum of θ_K at the L_3-edge, including fine features, was reproduced by the quantum resonant scattering calculation with the configuration interaction model. We also found the polarization dependence of θ_K.

Nevertheless, intrinsically, MOKE is described by two parameters, θ_{K} and the ellipticity (ε_{K}) that are derived from the optical rotation and MCD, respectively. In the final topic, to discuss not only θ_{K} but also ε_{K}, which is difficult to be observed by the existing resonant MOKE method in the soft X-ray energy region, we developed a new soft X-ray source with a polarization modulation at SPring-8 BL07LSU fully utilizing the feature of a segmented cross undulator. Its performance was confirmed by the XMCD measurements with the modulated light, then, we also developed a new magneto-optical method by combing the modulated soft X-ray and resonant MOKE. It enabled us to measure both of θ_{K} and ε_{K} simultaneously with high accuracy. We also determined the complex permittivity of the buried Fe film for the first time in the soft X-ray energy region.

Acknowledgements

It is my great pleasure to express my special gratitude to the following people for my doctoral thesis.

First of all, I would like to express my deepest gratitude to my supervisor, Prof. Iwao Matsuda, who has guided me to the exciting and splendid world of physics. I am very grateful to him that I could study on this subject and for his continuous advice and encouragement throughout my doctor course. His deep understanding of physics, exceptional experimental expertise, and dedicated working attitude have set a good example of an experimental physicist for me. I feel lucky to have him as my advisor.

I also would like to thank Prof. Hiroki Wadati for his collaboration on my research and a lot of useful advice on not only experiments but also future academic plans.

I am grateful to Dr. Susumu Yamamoto for his valuable advice on the experiments, writing manuscripts, and Dr. Koichiro Yaji for his a lot of useful advice.

I would like to thank Mr. Shingo Yamamoto as not only a collaborator but also a friend. He also helped me whether business and personal.

I am also grateful to Mr. Takashi Someya for his collaborating on our MOKE study and wonderful time to talk with him, and Dr. Ryu Yukawa for his a lot of valuable advice and taking care of me, and Dr. Baojie Feng and Ms. Ro-Ya Liu for their help with our ARPES study at Elettra, and Dr. Jiayi Tang, Mr. Kazushi Fujikawa, Mr. Kazuma Akikubo, Mr. Suguru Ito, and Ms. Kaori Takeuchi for their help and taking care of the group members.

With respect to our study on topological insulator, I would like to thank Dr. Koichi Murata for valuable discussion and providing the samples. I am also grateful to Prof. Kang L. Wang, Prof. Caroline A. Ross, and Dr. Mehmet Cengiz Onbasli for proving the samples and for critical reading of its manuscript. I would like to give special thanks to Prof. Shigemasa Suga for his wonderful advice on writing the manuscript. I also grateful to Dr. Kenichi Ozawa for his support for the ARPES measurement and valuable advice on the manuscript, and Dr. Paolo Moras, Dr. Polina Sheverdyaeva, and Dr. Sanjoy Kr Mahatha have given me a lot of experimental support. I am vey grateful to Dr. Tetsuroh Shirasawa for his making the samples and a lot of advice on the manuscript. I also thank Dr. Naoya Fukui and Prof. Shuji Hasegawa for their assistance in the sample preparation, and Prof. Akio Kimura for valuable discussion. This study was partially

supported by the Ministry of Education, Culture, Sports, Science, and Technology of Japan (X-ray Free Electron Laser Priority Strategy Program and Photon and Quantum Basic Research Coordinated Development Program) and performed using facilities of the Synchrotron Radiation Research Organization, The University of Tokyo (Proposal No. 2014B7473, 2015B7401, 2015A7401, 2014B7401, 2014A7401).

With respect to our study on MOKE, I would like to give special thanks to Dr. Munetaka Taguchi for the quantum calculation and valuable discussion with him. I also very grateful to Dr. Yasuyuki Hirata for his support for MOKE experiments and valuable discussion, and Dr. Kou Takubo, Mr. Masami Fujisawa, Mr. Yuichi Yokoyama, Mr. Kohei Yamamoto for their help to do measurements. I am vey thank Ms. Mihoko Araki for her help with the experiments and my daily lives at SPring-8. I would like to thank Prof. Masakiyo Tsunoda and Prof. Takeshi Seki for providing the Fe film and the FePt film, respectively, and Prof. Takashi Tanaka, Dr. Ryota Kinjo, Dr. Akihiro Kagamihata, Dr. Takamitsu Seike, Dr. Masao Takeuchi for developing the polarization modulated soft X-ray at SPring-8 BL07LSU. I also very grateful to Prof. Shik Shin for giving me the invaluable opportunities of MOKE experiments at SPring-8 BL07LSU. This work was partially supported by the Ministry of Education, Culture, Sports, Science, and Technology of Japan (X-ray Free Electron Laser Priority Strategy Program and Photon and Quantum Basic Research Coordinated Development Program) and the Asahi Glass Foundation. The experiments were performed using facilities of the Synchrotron Radiation Research Organization, The University of Tokyo (Proposal No. 2014A7401, 2014B7401, 2014B7473, 2015A7401, 2015B7401, 2016A7403, 2016A7504, 2016B7403). I also thank Prof. Masato Kotsugi for valuable discussion and Dr. Hiroshi Narita for building the experimental equipment. Mr. Valerio Lollobrigida and Mr. Yoshinobu Takahashi are acknowledged for his support during the experiments.

I would like to thank Prof. Yoshihisa Harada and Dr. Jun Miyawaki for their collaborating on the topological insulator and MOKE studies at SPring-8 BL07LSU, and Dr. Rei Hobara for his assistance in the topological insulator sample preparation and a lot of help with electronic systems and computer programs in the modulated MOKE study.

I am very grateful to Prof. Masaharu Oshima, Dr. Hideharu Niwa, Dr. Hisao Kiuchi, Dr. Yitao Cui, Mr. Kosuke Yamazoe, Mr. Junki Nakajima, Mr. Naoki Itamoto, Mr. Takanobu Inoue, Mr. Hao Wang, Mr. Tomoyuki Tsuyama, Ms. Misa Harada, Ms. Yuka Kosegawa, Ms. Yukimi Yamamoto, Ms. Emi Harada, and Ms. Emi Mitsuda. They have spared a great deal of time for helping me at SPring-8.

I also would like to thank Dr. Kenta Kuroda, Dr. Takeshi Suzuki, Ms. Ayumi Harasawa, Mr. Hirofumi Kudo, Ms. Akiko Fukushima, Ms. Motoko Yoshizawa, Ms. Yumiko Aihara, Ms. Kuniko Ikeda, Ms. Yumiko Tsutsumi, Ms. Yoshie Kaneko, and Ms. Akiko Hayashi for a lot of help with my research at Kashiwa.

I would like to express my special thanks to Prof. Fumio Komori and his group members: Dr. Toshio Miyamachi, Mr. Takushi Iimori, Mr. Norikazu Kawamura, Dr. Masamichi Yamada, Dr. Koichiro Ienaga, Dr. Sunghun Kim, Mr. Yukio Takahashi, Mr. Shuhei Nakashima, Mr. Takuma Hattori, Mr. Sogen Toyohisa. They brought me the precious chance to practice presentation skills at meetings.

I am also would like to thank Dr. Luca Castiglioni, Prof. Jürg Osterwalder, and Dr. Matthias Hengsberger, from whom I have been fortunate enough to receive tremendous guidance and knowledge on surface physics during my stay at Zürich, Switzerland as an oversea education. I also thank all members of Surface Science Group, University of Zürich for their kind help during my stay. Especially, the laser group members: Mr. Pavlo Kliuiev, Mr. Kay Waltar, Dr. Claude Monney, and Mr. Adrian Schuler gave me valuable advice. I would also like to thank secretaries of this group for great assistance to perform the research in comfort.

I wish to express my thanks to Prof. Tai-Chang Chiang for valuable discussion about topological insulator during his stay at The Institute for Solid State Physics (ISSP).

I need to thank Prof. Makoto Gonokami and Prof. Junji Yumoto who have been taking care of my course work of the Advanced Leading Graduate Course for Photon Science (ALPS) and giving valuable advice. I also acknowledge economical support from the ALPS programs of the University of Tokyo. I also would like to thank secretaries of this program and Gonokami-Yumoto-Ideguchi group for their help, and their members for discussion with them.

Finally, I would like to thank my family, especially, my parents for their kind support and understanding during all my studies.

December, 2016
Yuya Kubota

Contents

Chapter 1

Introduction

1.1 Background of the present study

Magnetism is one of the significant properties of condensed matters. The research has led us deep understanding of our nature and the application has become highly necessary in our society. Experimentally, light or an electromagnetic wave has been used as a probe to investigate magnetic materials. With visible light, we have been able to see various magneto-optical effects, such as the Faraday effect [1] and the magneto-optical Kerr effect (MOKE) [2–4]. When the probing photon energy increases up to the vacuum ultraviolet (VUV) $\sim$ X-ray region, the spectroscopic information becomes element-specific since it energetically covers absorption edges of the composing elements in a material. Since the X-ray absorption spectroscopy (XAS) requires a simple measurement set-up of electron yield, the XAS experiments have been carried out over the world. Moreover, the theoretical development of X-ray magnetic circular dichroism (XMCD), which is a phenomenon derived from the difference of the absorption between left- and right-circular polarized light (LCP and RCP) depending on magnetism, has now allowed researchers to evaluate the spin and orbital magnetic moments of the magnetic elements of a sample [5–7].

The XMCD approach has nowadays applied to the novel spintronics materials, such as heterostructures of magnetic and topological insulators (TIs) [8–16]. However, it has been technically challenging to resolve their academic and industrial demands. This is partly due to the fact that conventional detection of the electron yield in XMCD is rather surface sensitive [17] and, on the other hand, the main concerns of the heterostructures are magnetic properties of the buried film and the interface. Thus, innovations in measurement of the X-ray magneto-optical effect have been highly called for.

In addition to XMCD, MOKE using a resonant enhancement, so-called resonant MOKE, has also been mostly applied to the transversal MOKE (T-MOKE) geometry in the soft X-ray energy region [18, 19]. Since the reflected light from a sample is detected in MOKE measurement, it is a bulk sensitive method, thus, can access the magnetism of buried layers. Furthermore, MOKE experiment enables us to investigate not only the magnetic circular dichroism (MCD) like as XMCD but also the optical rotation derived from the variation of the phase difference between LCP and RCP. Permittivity, which is one of the most important parameters describing magnetic properties of materials, can be determined completely only after measuring both of these two magneto-optical parameters. However, since T-MOKE shows only intensity variations of the reflection, these parameters are non-separable in its measurement. Although they can be investigated individually by using the Faraday effect [20, 21], its transmission experiment is not suitable to be operated in the soft X-ray region because of a strong interaction between light and materials.

On the other hand, in the polar- and longitudinal-MOKE (P- and L-MOKE) measurements, the light polarization changes from linearly to elliptically due to MCD and its plane rotates as a result of the optical rotation before and after reflection at a surface of magnetic material. In contrast to the Faraday effect measurement, these techniques can be operated as long as the sample can reflect the incident light. Moreover, using the resonant enhancement in the VUV $\sim$ soft X-ray region, the optical rotation angle (the Kerr rotation angle, θ_{K}) becomes significantly larger than that obtained by visible light [22–29], as shown in Figs. 1.1(a) and (b). Some theoretical studies were also reported phenomenologically and by the first-principles calculations [21, 24, 25, 30, 31]. Figure 1.1(c) shows the θ_{K} spectrum obtained by the first-principles calculation. However, as one can see, there still remains a discrepancy in the θ_{K} values between experiment and theory, especially respect to quantum mechanism.

Furthermore, there is one more problem to determine the permittivity that it is more difficult to measure the ellipticity (ε_{K}) of the elliptically polarization than θ_{K} by the conventional technique in the VUV $\sim$ soft X-ray region [28]. In the visible energy region, MOKE measurement is performed with a polarization modulated incident light [33]. This method enables us to measure θ_{K} and ε_{K} not only simultaneously

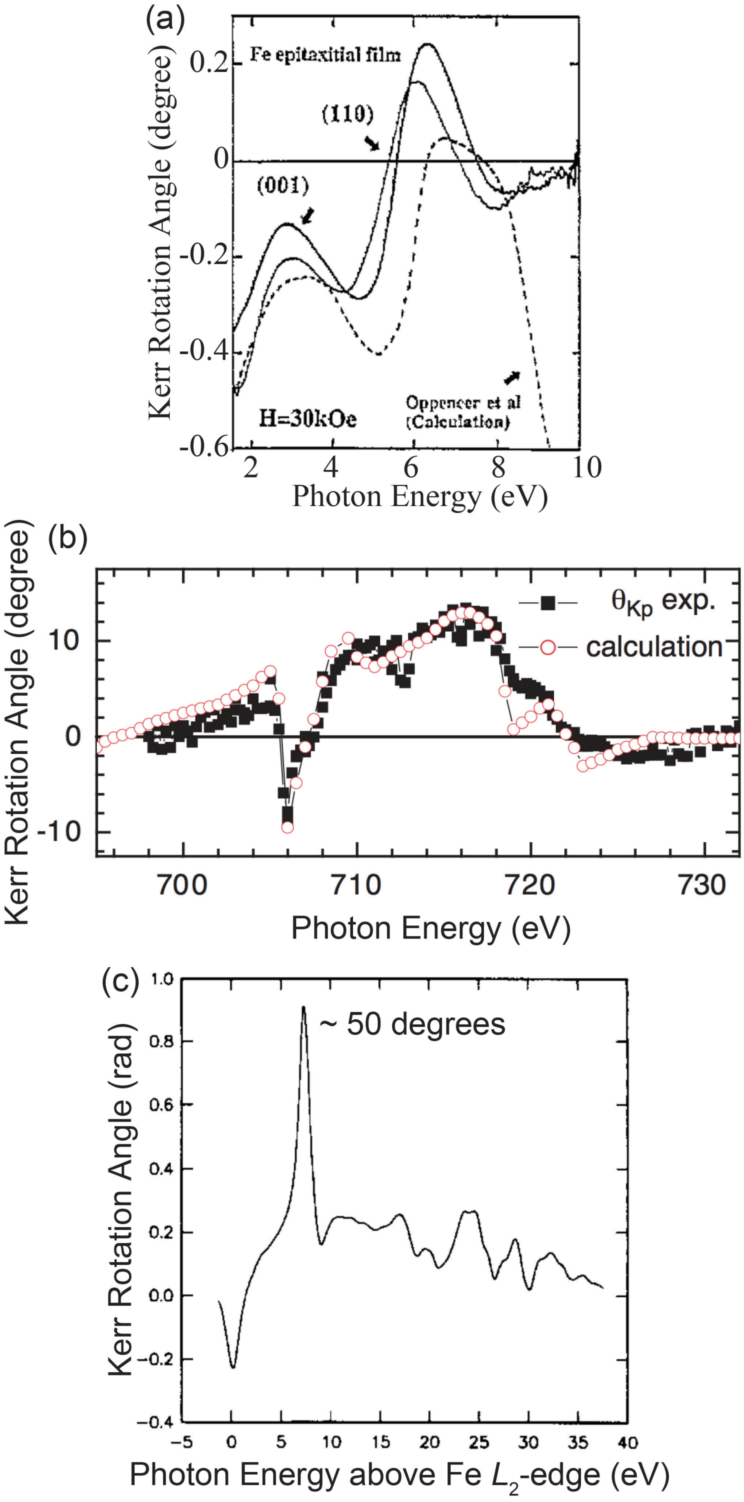

FIGURE 1.1: (a) The Kerr rotation angle (θ_K) spectra of Fe(001) and Fe(110) films at the visible photon energy region. The dashed line shows the theoretical spectrum. Taken from Ref. [32]. (b) The θ_K spectra of an Fe film at the L-edge. The filled squares and open circles represent the experimental and theoretical values, respectively. Taken from Ref. [25]. (c) The θ_K spectrum of Fe at the L_2-edge obtained by the first-principles calculation. Taken from Ref. [30].

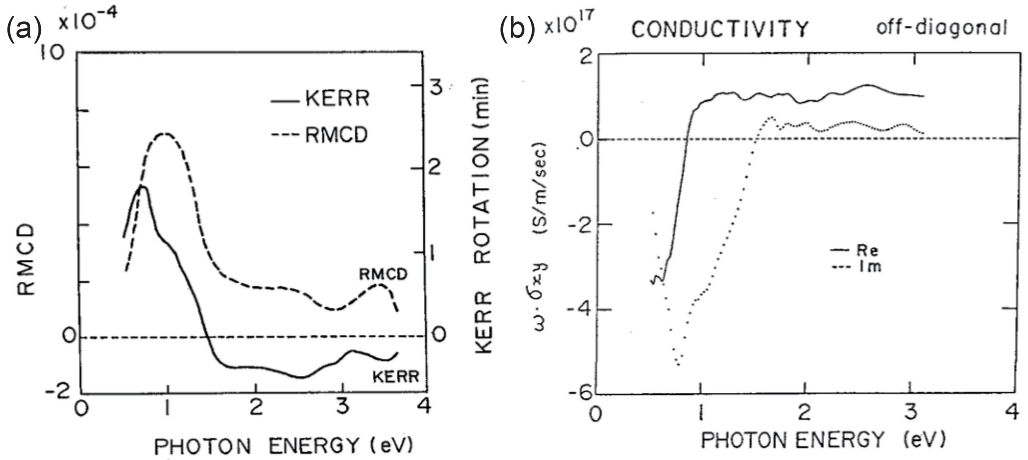

FIGURE 1.2: (a) The Kerr rotation angle (θ_K) and reflectance magnetocircular dichroism (RMCD) spectra of $\mathrm{Fe_2Se_8}$ at room temperature (RT). (b) Real and imaginary parts of off-diagonal element of conductivity tensor of $\mathrm{Fe_2Se_8}$ at RT. Taken from Ref. [34].

but also accurately, thus determine the permittivity completely. Figure 1.2 shows an example of results obtained by the MOKE measurement with the modulated visible light [34]. From the values of θ_K and reflectance magnetocircular dichroism (RMCD), which is proportional to ε_K, the real and imaginary parts of off-diagonal element of conductivity tensor that have magnetic information can be calculated. Conductivity has the mostly same information as permittivity and they can be transformed to each other easily.

However, it is difficult to realize a polarization modulated synchrotron radiation (SR) using conventional undulators. To get a proper understanding of the magneto-optical effect and the permittivity completely, it is required that a new SR source with the modulation using a new undulator and a new method to measure θ_K and ε_K simultaneously.

1.2 Purpose of the present study

The main purpose of this thesis is to unveil the magnetism of buried layers. Furthermore, to realize it, we develop a new soft X-ray source with the polarization modulation and a new method combining the new light source and the magneto-optical effect.

At first, we focused on an interesting magnetism of the buried interface between a three dimensional (3D) TI, $\mathrm{Bi_2Se_3}$, and a magnetic material, $\mathrm{Y_3Fe_5O_{12}}$ (YIG). It was reported that Bi_2Se_3 shows a magnetic order at the interface due to the proximity effect even at $T = 130$ K by visible MOKE and transport measurements [13]. To understand its mechanism, we investigated the interface by angle-resolved photoelectron spectroscopy (ARPES) and XMCD measurements with fixed polarizations. The interesting issues in this study are as follows:

- Does Bi_2Se_3 make Dirac-like surface states at the surface and the interface even grown on YIG?
- What mechanism generates the proximity effect at the interface? Is it possible that the magnetic order of TI realizes above RT?

From the conclusion of the first topic, we considered that investigating magnetism of buried layers requires a bulk sensitive method with high accuracy. Therefore, in second topic, we focused on resonant MOKE and studied it using a buried Fe film for the *s*- and *p*-polarized SR at the *L*-edge to get a proper understanding. The values of θ_K obtained from the experiment were compared with that obtained from two types of simulations: one is based on classical electromagnetic theory, and the other is the quantum resonant scattering calculation. We discuss on the following problems:

- What shape of θ_K spectrum can be observed with a smaller influence of the capping layer than that of previous studies [24, 25] at the Fe *L*-edge? How does it depend on the polarization of incident light?
- What quantum mechanism controls resonant MOKE? What makes the discrepancy between experiment and theory, as shown in Fig. 1.1?

The third objective is a development of the new soft X-ray source with the polarization modulation by fully utilizing the feature of a segmented cross undulator at SPring-8 BL07LSU. Furthermore, we considered the new method combing the new soft X-ray and the resonant MOKE measurement with the rotating-analyzer ellipsometry (RAE) to get new information of buried magnetic layers.

Finally, as a main subject of this thesis, we realized the resonant MOKE measurement for the buried Fe film with the polarization modulated soft X-ray. The central issues of this study are as follows:

- How can θ_K and ε_K be observed simultaneously in the soft X-ray energy region?

- What values of permittivity of the buried Fe film is determined that nobody has succeeded in doing in the soft X-ray energy region?

1.3 Structure of this thesis

Chapter 2 describes the basic principles of the magneto-optical effect and spintronics materials used in this thesis. In the section of the magneto-optical effect, I focus on MCD and MOKE for using in experiments. $3d$ transition magnetic materials and topological materials are described as the spintronics materials that are employed as samples in our studies.

Chapter 3 describes light sources and conventional experimental methods. SR from the VUV to the soft X-ray energy region was used as a light source in this thesis. To observe a band structure directly, ARPES experiment was operated at the VUV-Photoemission beamline at Elettra, Italy. In addition, XMCD and MOKE measurements were performed at the Fe L-edge at SPring-8 BL07LSU to discuss magnetic properties. Especially, the MOKE measurements were used the resonant enhancement at the absorption edges with the RAE.

Chapter 4 describes the study of an interface between a 3D TI, Bi_2Se_3, film and a ferrimagnetic insulator, YIG, film. This material is expected that the magnetic TI appears at the interface by the proximity effect. From ARPES and XMCD measurements, we proposed the model of the proximity effect at the interface.

In Chapter 5, the L-edge resonant MOKE of a buried Fe film was investigated. θ_{K} was measured for the s- and p-polarized incident soft X-rays. The experimental values were compared with the calculation values obtained from two methods: one is based on the phenomenological theory with empirical optical constants, and the other is the simulation based on the quantum resonant scattering theory with the configuration interaction (CI) model.

The main subjects of this thesis are a development of a polarization modulated soft X-ray and an adapting this light source to the magneto-optical effect. The detail of this development of the polarization modulation at SPring-8 BL07LSU is described in Chapter 6. In addition, the XMCD measurements with this modulated light source for magnetic materials were made to estimate the performance of this soft X-ray.

Furthermore, the polarization modulated soft X-ray was combined and the resonant MOKE measurement with the RAE in Chapter 7. In this resonant MOKE measurement, θ_{K} and ε_{K} can be measured simultaneously and accurately. Chapter 7 describes the detail of this method and shows the results of resonant MOKE with the modulation for the buried Fe film. Therefore, the element-specific complex permittivity of Fe was determined for the first time in the soft X-ray energy region.

Finally, Chapter 8 is devoted to summary and future prospects.

Chapter 2

Basic principles

2.1 Magneto-optical effect

First, I shall define left-circular polarized light (LCP) and right-circular polarized light (RCP) used in this thesis. Figure 2.1 shows the definition of LCP, RCP, the helicity+ (σ^+), and the helicity$-$ (σ^-) of light. LCP (RCP) that has the helicity+($-$) is defined as that the electric field vector turns counterclockwise (clockwise) when the observer is facing in the on-coming light.

The magneto-optical effect is a phenomenon where light and a magnetic material interact with each other. The origin of the magneto-optical effect is shown in Fig. 2.2. The trajectory of the electric field of linear polarized light is expressed by a superposition of LCP and RCP with the same amplitude and rotating velocity, as shown in Fig. 2.2(a). After interaction with a magnetic material, if a phase difference between LCP and RCP is generated, the polarization plane of the linear polarized light rotates, as shown in Fig. 2.2(b). This phenomenon is called the optical rotation. As shown in Fig. 2.2(c), if a difference of amplitude between the electric fields of LCP and RCP

FIGURE 2.1: Definition of circular polarization and the helicity.

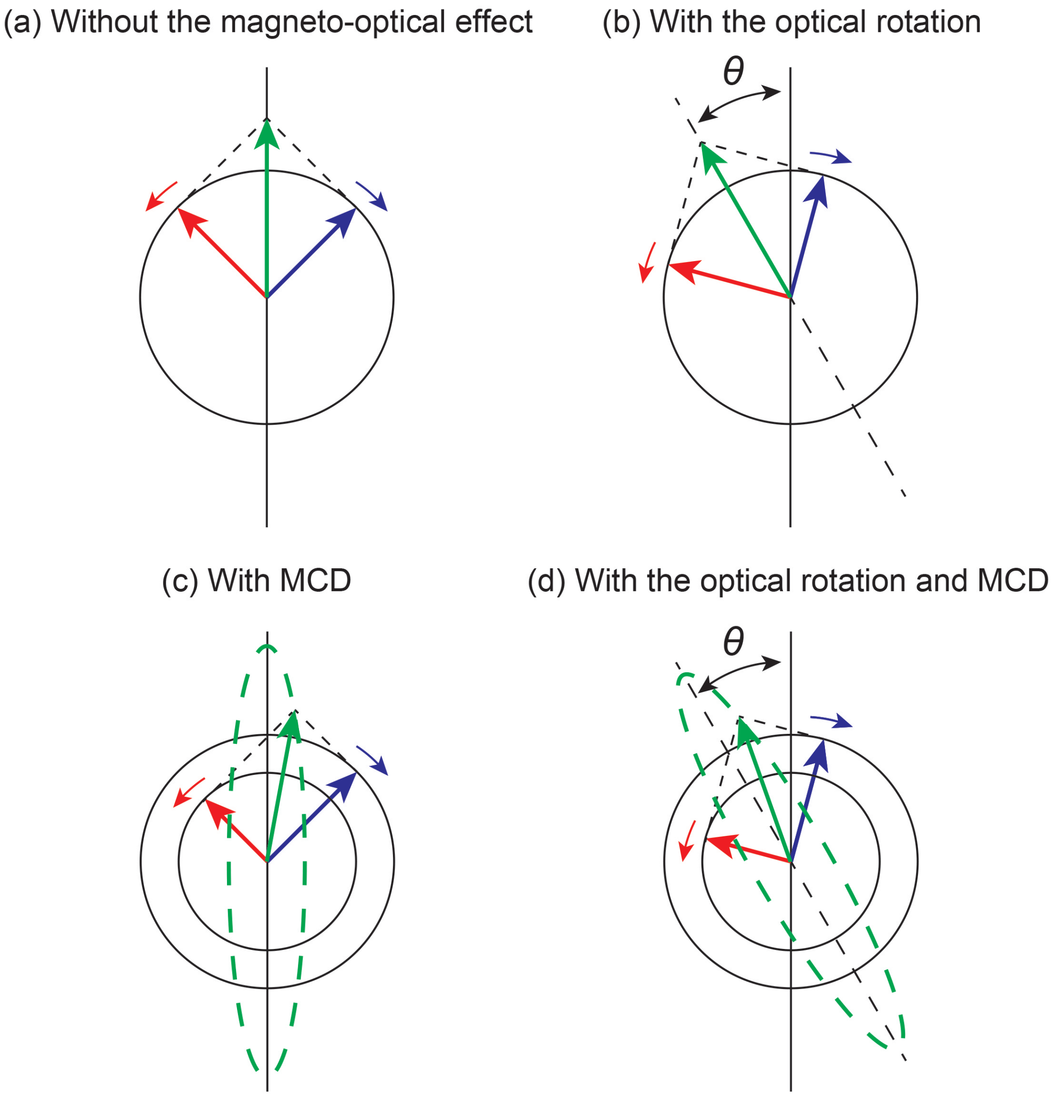

FIGURE 2.2: Schematic drawing of the origin of the magneto-optical effect. θ represents the optical rotation angle.

is generated, that is called the magnetic circular dichroism (MCD), the linear polarization varies to an elliptically polarization. When both of the optical rotation and MCD are observed, the light interacted with the magnetic material has the elliptically polarization and its plane rotates, as shown in Fig. 2.2(d).

There are some kinds of the magneto-optical effects, such as MCD, the Faraday effect [1], the magneto-optical Kerr effect (MOKE) [2–4], and the magnetic double refraction [35]. In this section, I describe MCD, especially X-ray MCD (XMCD), and MOKE that were discussed in this thesis.

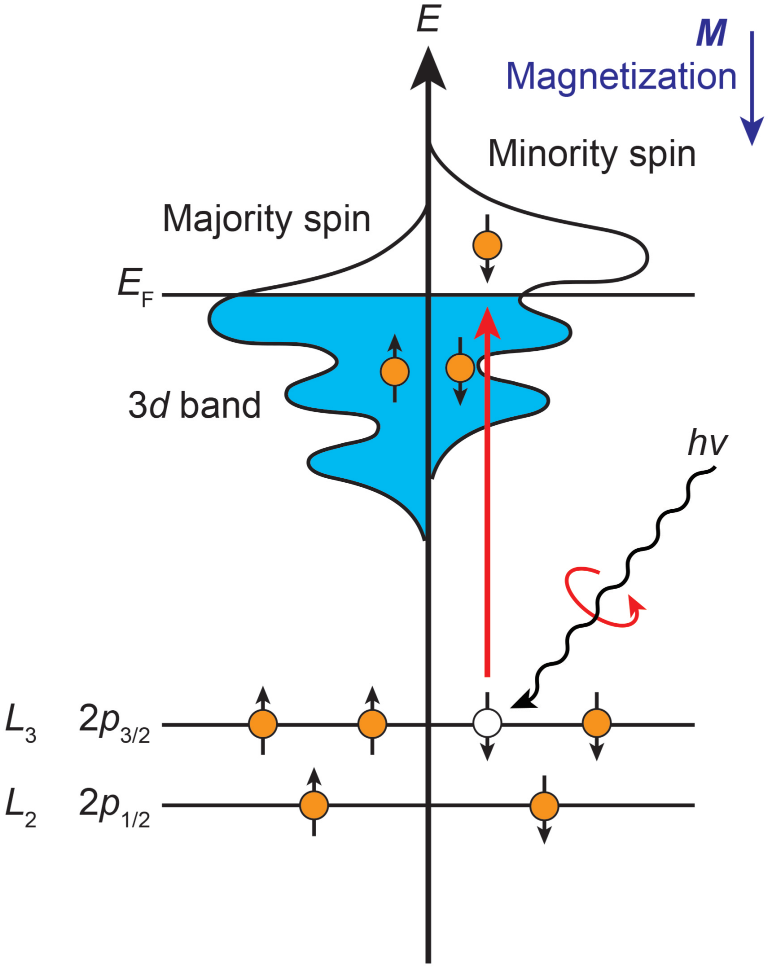

FIGURE 2.3: Schematic drawing of the $2p \rightarrow 3d$ optical transition in a magnetic material. The directions of magnetization ($\boldsymbol{M}$) and the majority spin are antiparallel. E_{F} represents the Fermi energy.

2.1.1 Magnetic circular dichroism (MCD)

As mentioned above, MCD is a phenomenon that a magnetic material shows a difference of photo-absorption between LCP and RCP. When X-ray is used as an incident light, MCD can be observed at the absorption edges and it reflects the spin states of the magnetic samples. Here, I shall focus on this XMCD, especially, the $2p \rightarrow 3d$ optical transition because the $3d$ electrons play the central role in the magnetism of transition magnetic metals, thus, it is most widely used in XMCD measurements.

Figure 2.3 shows the optical transition of $2p \rightarrow 3d$ in a magnetic material. By the exchange interaction, the $3d$ state splits to the majority spin state (up spin) and the minority spin state (down spin). After a $2p$ electron is excited by LCP or RCP, which has a parallel or antiparallel direction to that of the magnetization, a $2p$ hole is generated and the $2p$ state splits to the $2p_{3/2}$ and $2p_{1/2}$ states by the spin-obit (SO) interaction. At the $2p_{3/2}$ ($2p_{1/2}$) state, the spin angular momentum $\boldsymbol{S}$ and the orbital angular momentum $\boldsymbol{L}$ are parallel (antiparallel). Using the Clebsch-Gordan coefficients, the spherical harmonics Y_l^m, and the spin functions α, β, the angle parts of wave functions of the $2p_{3/2}$ and $2p_{1/2}$ states are expressed as

$$2p_{3/2}$$

$$|jm_j\rangle = \begin{cases} |\frac{3}{2},\frac{3}{2}\rangle \propto Y_1^1\alpha \\ |\frac{3}{2},\frac{1}{2}\rangle \propto \sqrt{\frac{2}{3}}Y_1^0\alpha + \sqrt{\frac{1}{3}}Y_1^1\beta \\ |\frac{3}{2},\frac{-1}{2}\rangle \propto \sqrt{\frac{1}{3}}Y_1^{-1}\alpha + \sqrt{\frac{2}{3}}Y_1^0\beta \\ |\frac{3}{2},\frac{-3}{2}\rangle \propto Y_1^{-1}\beta, \end{cases} \tag{2.1}$$

$$2p_{1/2}$$

$$|jm_j\rangle = \begin{cases} |\frac{1}{2},\frac{1}{2}\rangle \propto -\sqrt{\frac{1}{3}}Y_1^0\alpha + \sqrt{\frac{2}{3}}Y_1^1\beta \\ |\frac{1}{2},\frac{-1}{2}\rangle \propto -\sqrt{\frac{2}{3}}Y_1^{-1}\alpha + \sqrt{\frac{1}{3}}Y_1^0\beta. \end{cases} \tag{2.2}$$

Under the electric dipole approximation, the spin state is conserved and the z component of the electric orbital angular momentum excited by σ^+ increases by 1 ($\Delta m_l = +1$). On the other hand, σ^- beam decreases m_l by 1 ($\Delta m_l = -1$).

Figure 2.4 shows a schematic drawing of the relative transition probabilities in the $2p \rightarrow 3d$ optical transition with the exchange and SO interactions in the $3d$ state. Here, I assume that the radial parts of wave functions of the $2p_{3/2}$ and $2p_{1/2}$ states can be equal, and the majority $3d$ spin state is fully occupied to discuss simply. The relative transition probability by circular polarized light is calculated by using the Gaunt coefficients $c^1\left(2m_d, 1m_p\right)$

$$|\left\langle 2m_d|\hat{\boldsymbol{r}}_{\pm}|1m_p\right\rangle|^2 = \left|\left\langle 2m_d \left| \frac{x \pm iy}{\sqrt{2}r} \right| 1m_p \right\rangle\right|^2 = |c^1\left(2m_d, 1m_p\right)|^2. \tag{2.3}$$

Defining the number of holes at the m_d state as h_{m_d}, the expectation values of L_z and S_z are calculated as

$$\langle L_z\rangle = -\left(2h_{+2} + h_{+1} - h_{-1} - 2h_{-2}\right)\hbar, \tag{2.4}$$

$$\langle S_z\rangle = \left(h_{+2} + h_{+1} + h_0 + h_{-1} + h_{-2}\right)\frac{\hbar}{2}. \tag{2.5}$$

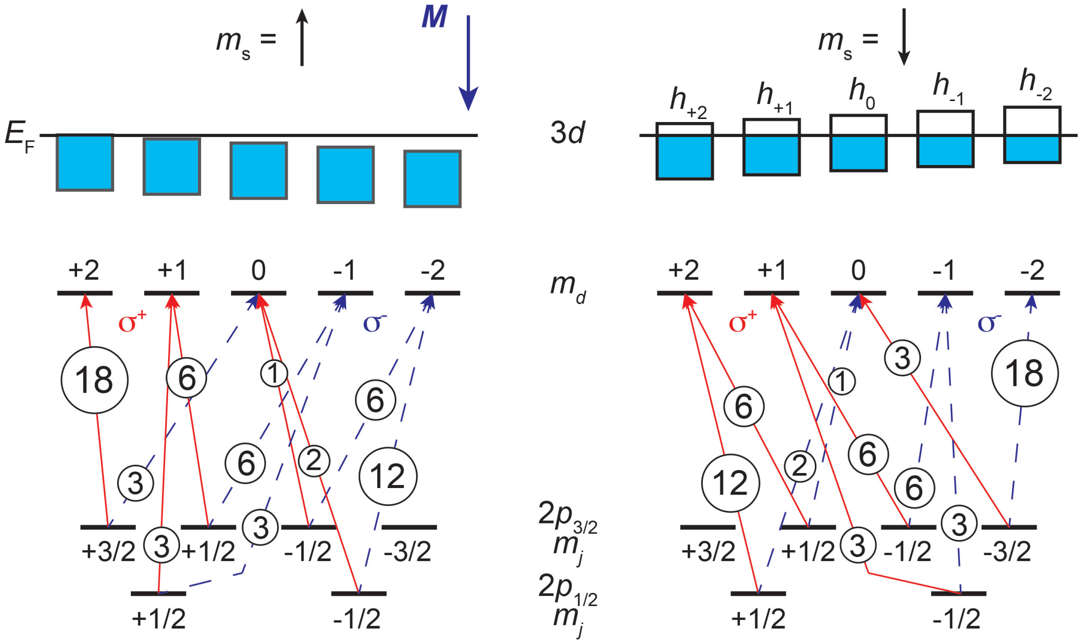

FIGURE 2.4: Schematic drawing of the relative transition probabilities and the energy levels in the $2p \to 3d$ optical transition by σ^+ or σ^- with the exchange and SO interactions in the $3d$ state. The blue squares represent the one electron occupation probabilities.

The intensity of relative optical transition is proportional to the product of h_{m_d} and the transition probabilities, as shown in Fig. 2.4. Therefore, we obtain the intensity of the $2p \to 3d$ relative optical transition by σ^+ and σ^-

$$L_3: \ \Delta I_{L_3} \propto 6h_{+2} + 6h_{+1} + 2h_0 - 6h_{-1} - 18h_{-2}, \tag{2.6}$$

$$L_2: \ \Delta I_{L_2} \propto 12h_{+2} + 3h_{+1} - 2h_0 - 3h_{-1}, \tag{2.7}$$

and

$$\Delta I_{L_3} + \Delta I_{L_2} \propto 9\left(2h_{+2} + h_{+1} - h_{-1} - 2h_{-2}\right) \propto -9\left\langle L_z \right\rangle. \tag{2.8}$$

If there is no SO interaction at the $3d$ state, that is to say, h_{m_d} = const. and $\langle L_z \rangle = 0$, we can obtain $\Delta I_{L_3} = -\Delta I_{L_2}$, thus, the XMCD absorption spectrum like as Fig. 2.5(a) is observed. However, ordinarily, the SO interaction works at the $3d$ state ($\langle L_z \rangle \neq 0$). The absolute values of XMCD integral at the L_3- and L_2-edges are not equal ($\Delta I_{L_3} \neq -\Delta I_{L_2}$) and the XMCD spectrum shapes like as Fig. 2.5(b).

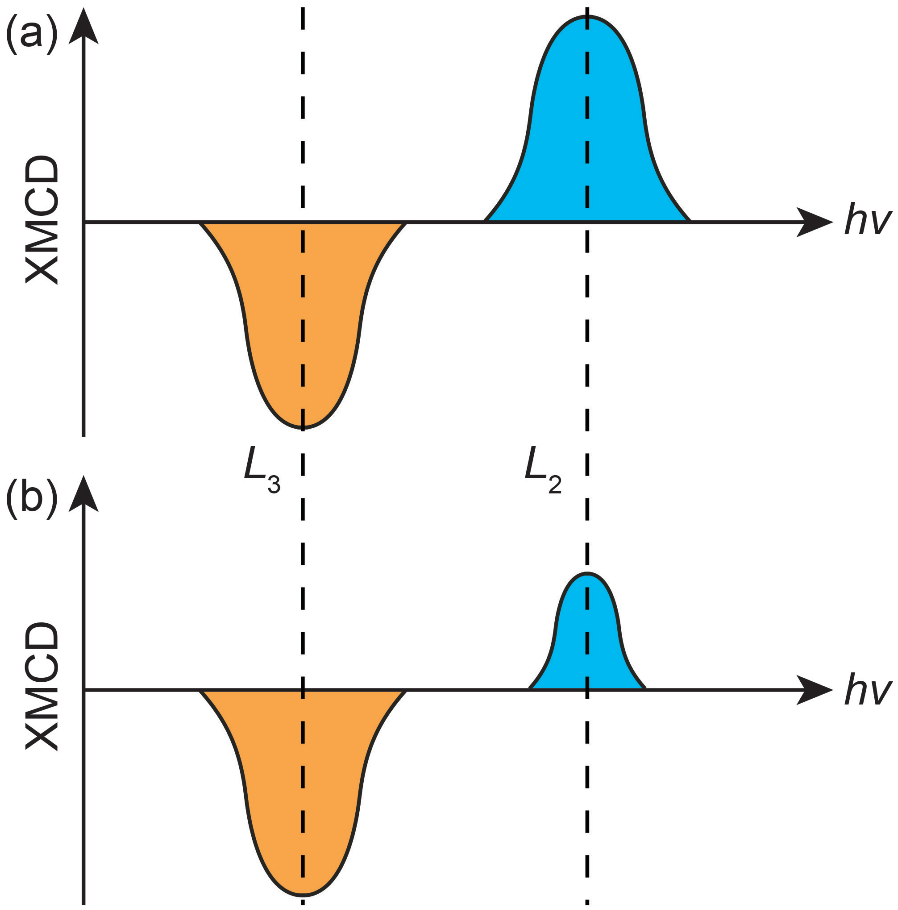

FIGURE 2.5: Schematic drawing of the XMCD absorption spectra at the L-edge without the SO interaction (a) and with the SO interaction (b) at the $3d$ state. The absolute values of XMCD integral at the L_3- and L_2-edges are equal in (a) or not equal in (b).

2.1.2 Magneto-optical Kerr effect (MOKE)

MOKE is one of the popular phenomena where photon and magnetic materials interact with each other. MOKE is classified into three types by its geometry, the polar MOKE (P-MOKE), the longitudinal MOKE (L-MOKE), and the transverse MOKE (T-MOKE), as shown in Fig. 2.6. In this thesis, the surface normal of a magnetic material can be chosen parallel to the z-axis and the plane of incidence as the yz-plane. The directions of magnetization are parallel to the z-, y-, and x-axes for P-, L-, and T-MOKE, respectively. In P- and L-MOKE, the light polarization changes from linearly to elliptically and its plane rotates before and after reflection at the surface of a magnetic material, as shown in Fig 2.6(a). Its rotation angle is defined as the Kerr

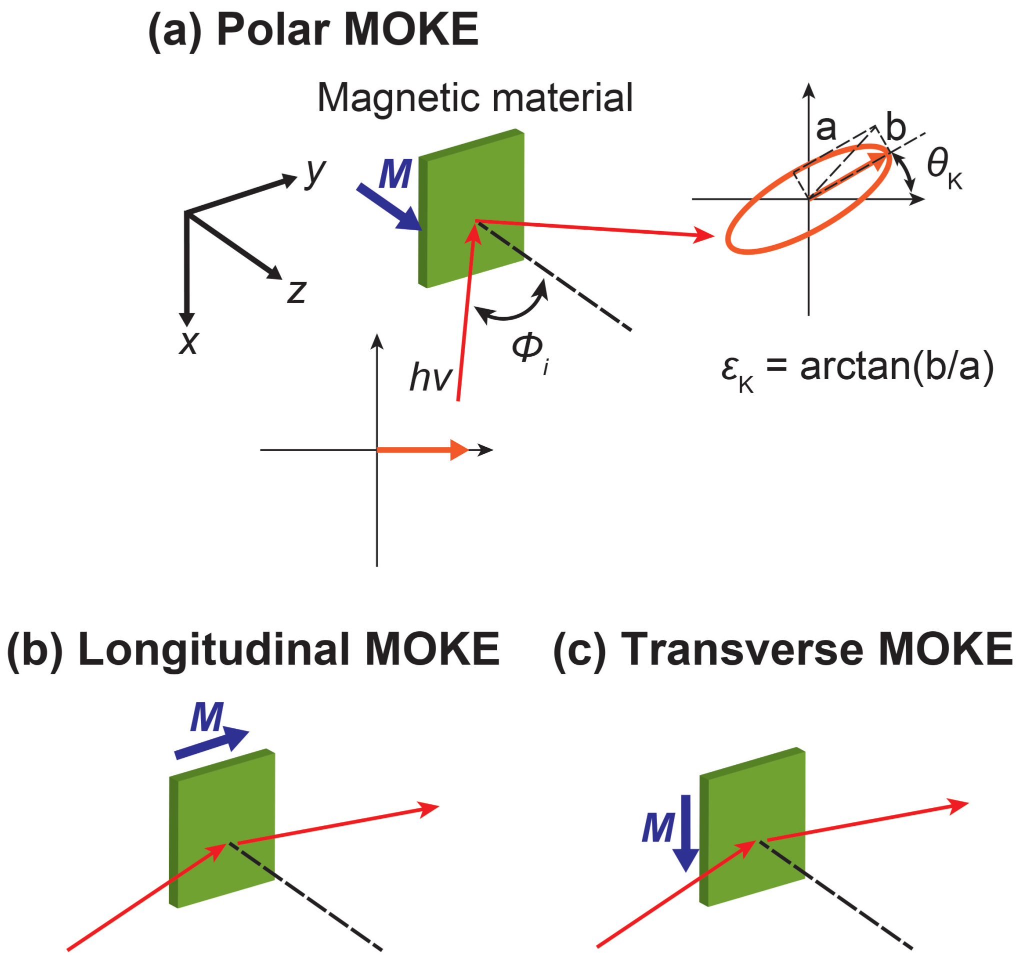

FIGURE 2.6: Schematics of the geometries of the polar (a), longitudinal (b), and transverse (c) MOKE.

rotation angle (θ_K) and the ellipticity (ε_K) is defined as

$$\varepsilon_\mathrm{K} = \arctan \frac{b}{a}, \tag{2.9}$$

where a and b are the long and short axes of the ellipse, respectively. Observation of θ_K and ε_K has been used to obtain magnetic information. On the other hand, T-MOKE shows only intensity variations of the reflected light depending on the magnetization.

Polar MOKE (P-MOKE)

P-MOKE is theoretically expressed by the complex Fresnel coefficients [4]

$$r_{ss} = (n_0 \cos\phi_i - n\cos\phi_t) \,/\, (n_0 \cos\phi_i + n\cos\phi_t)\,, \tag{2.10}$$

$$r_{pp} = (n \cos\phi_i - n_0\cos\phi_t) \,/\, (n \cos\phi_i + n_0\cos\phi_t)\,, \tag{2.11}$$

$$r_{ps} = \frac{-in_0\,(n_+ - n_-)\cos\phi_i}{(n\cos\phi_t + n_0\cos\phi_i)\,(n\cos\phi_i + n_0\cos\phi_t)\cos\phi_t}, \tag{2.12}$$

$$r_{sp} = r_{ps}. \tag{2.13}$$

r_{ij} means the ratio of the incident j-polarized electric field and the reflected i-polarized electric field. n (n_0) represents the complex refraction constant of the magnetic material (over layer) given by $n\,(n_0) = 1 - \delta_{1(0)} + i\beta_{1(0)}$. It is composed of a real part $1 - \delta_{1(0)}$ and an imaginary part $\beta_{1(0)}$ that represent non-magnetic dispersion and absorption, respectively. $n_\pm$ are expressed as $n_\pm = 1 - (\delta_1 \pm \Delta\delta) + i\,(\beta_1 \pm \Delta\beta)$, where the subscripted sign ± indicates that the directions of the photon helicity and magnetization are parallel/antiparallel in the sample, and $n = 1/2\,(n_+ + n_-)$. Here $\Delta\delta$ and $\Delta\beta$ denote the magnetic contributions of δ_1 and β_1, respectively. ϕ_i and ϕ_t are the angles of incidence and refraction, respectively. θ_K and ε_K for the s-polarized incident light (θ^s_K and ε^s_K) and the p-polarized incident light (θ^p_K and ε^p_K) in the P-MOKE geometry are expressed as [4]

$$\theta^s_\mathrm{K} + i\varepsilon^s_\mathrm{K} = -r_{ps}/r_{ss} \approx \frac{-in_0nQ}{\left(n^2 - n_0^2\right)}\left(\frac{\cos\phi_i}{\cos(\phi_i - \phi_t)}\right), \tag{2.14}$$

$$\theta^p_\mathrm{K} + i\varepsilon^p_\mathrm{K} = r_{sp}/r_{pp} \approx \frac{-in_0nQ}{\left(n^2 - n_0^2\right)}\left(\frac{\cos\phi_i}{\cos(\phi_i + \phi_t)}\right), \tag{2.15}$$

where the Voigt parameter Q for the P-MOKE geometry is given by $Q = (n_+ - n_-)\,/\,(n\cos\phi_t)$. Moreover, the permittivity tensor for the P-MOKE geometry is expressed as

$$\epsilon = \begin{pmatrix} \epsilon_{xx} & \epsilon_{xy} & 0 \\ -\epsilon_{xy} & \epsilon_{yy} & 0 \\ 0 & 0 & \epsilon_{zz} \end{pmatrix}, \tag{2.16}$$

and Q is also given by $Q = i\epsilon_{xy}/\epsilon_{xx}$.

Longitudinal MOKE (L-MOKE)

The complex Fresnel coefficients for L-MOKE are the same as those for P-MOKE except for r_{sp} [4],

$$r_{ss} = \left(n_0 \cos\phi_i - n\cos\phi_t\right) / \left(n_0\cos\phi_i + n\cos\phi_t\right), \tag{2.17}$$

$$r_{pp} = \left(n\cos\phi_i - n_0\cos\phi_t\right) / \left(n\cos\phi_i + n_0\cos\phi_t\right), \tag{2.18}$$

$$r_{ps} = \frac{-in_0\left(n_+ - n_-\right)\cos\phi_i}{\left(n\cos\phi_t + n_0\cos\phi_i\right)\left(n\cos\phi_i + n_0\cos\phi_t\right)\cos\phi_t}, \tag{2.19}$$

$$r_{sp} = -r_{ps}. \tag{2.20}$$

θ_{K}, ε_{K}, and the permittivity tensor for L-MOKE are expressed as

$$\theta_{\mathrm{K}}^{s} + i\varepsilon_{\mathrm{K}}^{s} = -r_{ps}/r_{ss} \approx \frac{-in_0 nQ}{\left(n^2 - n_0^2\right)}\left(\frac{\cos\phi_i\tan\phi_t}{\cos\left(\phi_i - \phi_t\right)}\right), \tag{2.21}$$

$$\theta_{\mathrm{K}}^{p} + i\varepsilon_{\mathrm{K}}^{p} = -r_{sp}/r_{pp} \approx \frac{-in_0 nQ}{\left(n^2 - n_0^2\right)}\left(\frac{\cos\phi_i\tan\phi_t}{\cos\left(\phi_i + \phi_t\right)}\right), \tag{2.22}$$

$$\epsilon = \begin{pmatrix} \epsilon_{xx} & 0 & \epsilon_{xz} \\ 0 & \epsilon_{yy} & 0 \\ -\epsilon_{xz} & 0 & \epsilon_{zz} \end{pmatrix}, \tag{2.23}$$

where Q for the L-MOKE geometry is given by

$$Q = \frac{n_+ - n_-}{n\sin\phi_t} = i\frac{\epsilon_{xz}}{\epsilon_{xx}}. \tag{2.24}$$

Transverse MOKE (T-MOKE)

In T-MOKE, the intensity variation of the reflected light depending on magnetism occurs for only the p-polarized wave. The reflection coefficients have the form

$$r_{pp}\left(M^{\pm}\right) \approx \bar{r}_{pp}\left[1 \pm \frac{\epsilon_0\epsilon_2\sin 2\phi_i}{\epsilon_1^2\cos^2\phi_i - \epsilon_0\epsilon_1 + \epsilon_0^2\sin^2\phi_i}\right], \tag{2.25}$$

where $\bar{r}_{pp}$ is the non-magnetic p-polarized reflection coefficient of the magnetic material and $\epsilon_0 = n_0^2$ [4]. ϵ_1 and ϵ_2 represent the diagonal and off-diagonal components of permittivity tensor, respectively.

2.2 Spintronics materials

In this section, I shall describe 3*d* transition magnetic materials and topological materials, especially, topological insulator (TI) as the representative materials that have been widely used in the fields of magnetism and spintronics. It is notable that the spin properties of 3*d* transition magnetic materials and TI are affected by the spin exchange interaction and the SO interaction, respectively.

2.2.1 3*d* transition magnetic materials

Elements in the *d*-block of the periodic table, which includes groups 3 to 12 on the periodic table, are called 3*d* transition metals. They have one or more *d*-orbital electrons as their outermost electrons. Especially, since Fe, Co, and Ni exhibit ferromagnetism at room temperature (RT), their pure metals and alloys have been attracting a wide interest in the magnetism and spintronics research fields for many years. Figure 2.7 shows the saturation magnetic moment per atom at $T = 0$ K of alloys including Fe, Co, or Ni as dependent on the average electron number per atom. This curve is called the

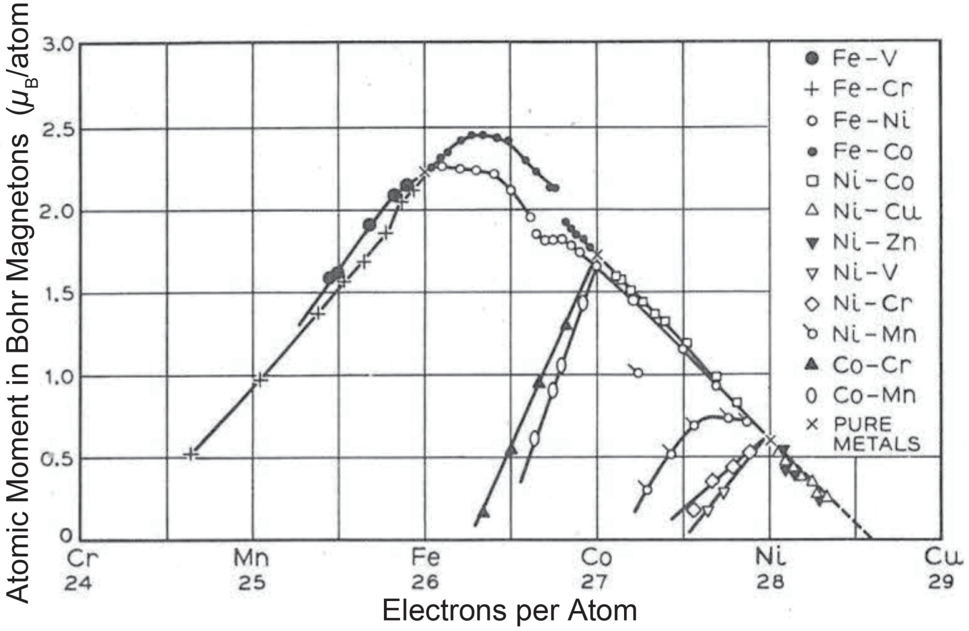

FIGURE 2.7: Saturation magnetization as dependent on electron concentration. Taken from Ref. [36].

Slater-Pauling curve. As one can see, this relation has regularity mostly independent on materials. The magnetic moments per atom of pure Fe, Co, and Ni are 2.2, 1.7, and 0.6 μ_B/atom, respectively.

$3d$ transition metals form $3d$ bands that determine their magnetic properties. Figure 2.8 shows the spin density of states of Ni (a) and Fe (b) obtained by the calculations. As one can see, the $3d$ band splits to the up spin state and the down spin state derived from the exchange interaction. The up spin state of Ni is occupied fully and there is only a limited number of holes in the down spin state. On the other hand, for Fe, the density of states (DOS) for up spin ($n_\uparrow$) is much larger than that for down spin ($n_\downarrow$). The difference between $n_\uparrow$ and $n_\downarrow$ corresponds to the magnetic moment, that is to say, $n_\uparrow - n_\downarrow = 0.6\ \mu_B$/atom for Ni, $n_\uparrow - n_\downarrow = 2.2\ \mu_B$/atom for Fe.

Finally, we show θ_K of representative examples of $3d$ transition magnetic metals and their alloys obtained by using visible light, as shown in Table 2.1.

TABLE 2.1: The Kerr rotation angle (θ_K) of representative examples of $3d$ transition magnetic metals and their alloys in the visible range at RT.

Material	θ_K (degree)	$h\nu$ (eV)	Ref.
Fe	0.87	0.75	[39]
Co	0.85	0.62	[39]
Ni	0.19	3.1	[39]
Fe_3O_4	0.32	1	[40]

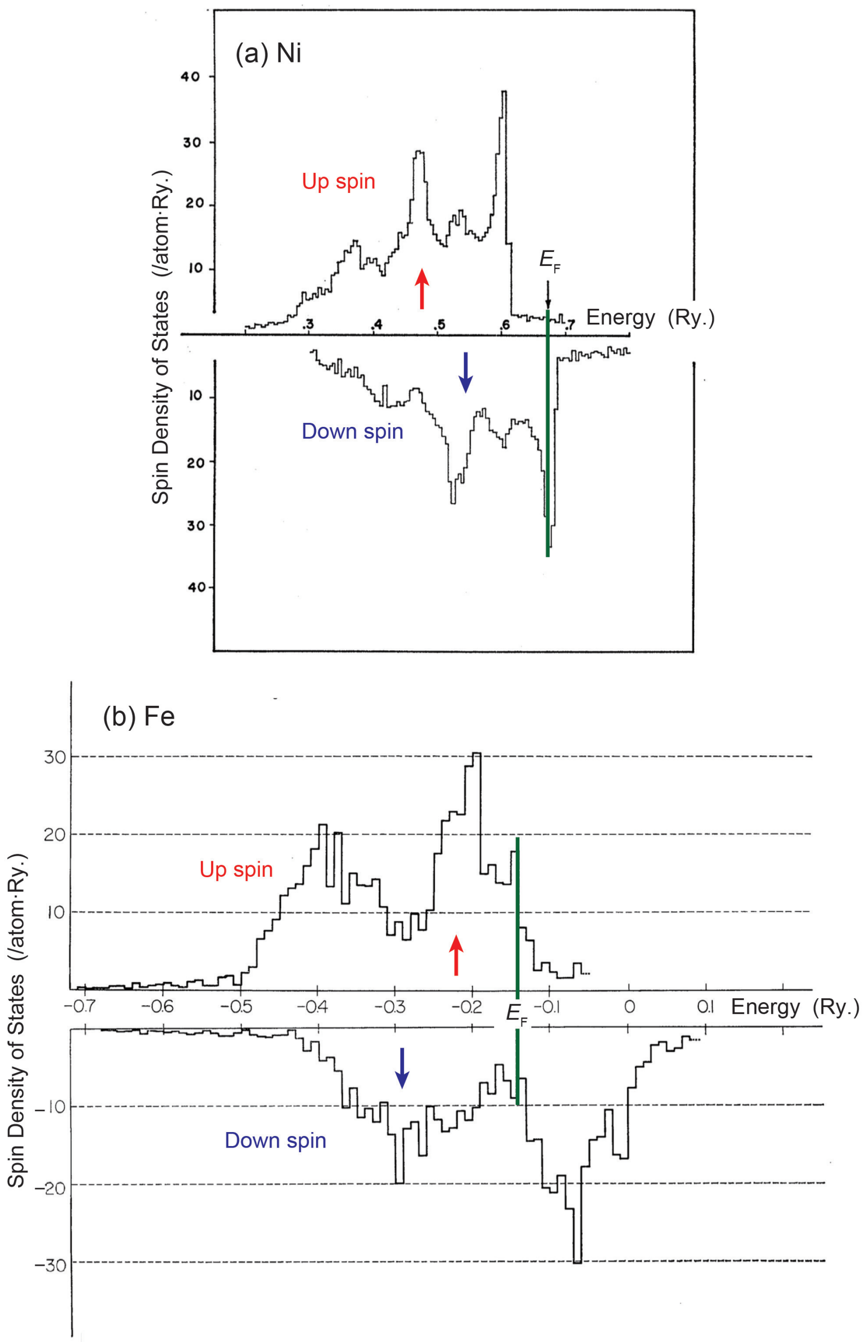

FIGURE 2.8: (a) Density of states (DOS) curves for up (upper) and down spins (bottom) of Ni. Taken from Ref. [37]. (b) DOS curves for up (upper) and down spins (bottom) of Fe. Taken from Ref. [38]. E_F represents the Fermi energy.

2.2.2 Topological materials

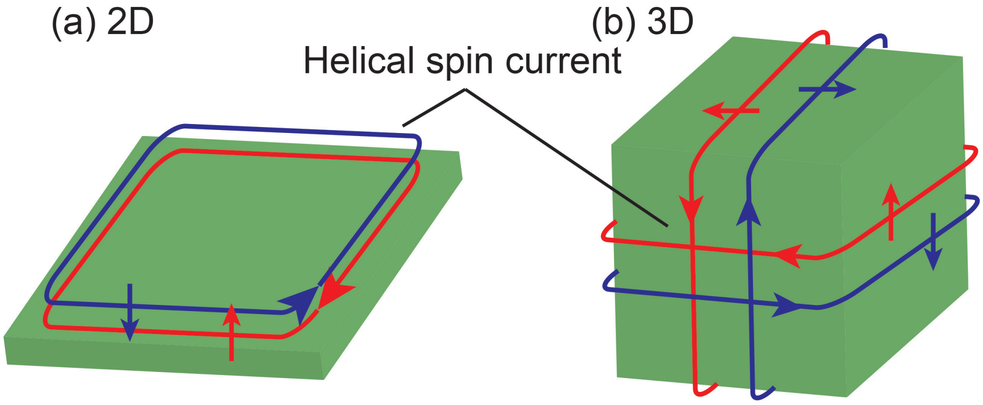

FIGURE 2.9: Schematic drawing of a 2D (a) and a 3D (b) TI.

TI was first proposed theoretically in 2005 [41–43]. TI is a quantum spin Hall system and realized in both of two dimensional (2D) [41–43] and three dimensional (3D) [44–46] systems, as shown in Fig. 2.9. Although TIs show bulk insulating performance, they exhibit gapless states at their edges (for 2D) and surfaces (for 3D). The edge or surface states are ensured by time-reversal symmetry (TRS) and the spin polarization of the edge or surface states electrons is locked to its momentum (helical spin current), as shown in Fig. 2.9.

Two dimensional topological insulator (2D TI)

Figure 2.10(a) shows a schematic drawing of the band structure of 2D TI. The gapless edge state connects the valence band with the conduction band of the bulk state (insulator). The band structure of the edge state is symmetric about $k = 0$, where k represents a wave number, and the symmetric points show opposite spin directions each other (the Kramers pair).

There is a number that describes the characteristic of TI, the Z_2 topological number [41, 47, 48]. The Z_2 topological number, ν, is defined below. Here, I shall consider that there are $2N$ bands (N: integer) below the Fermi energy (E_{F}), and they have Bloch eigenstates $|u_{n,\boldsymbol{k}}\rangle$ ($n = 1, 2, \cdots, 2N$). A $2N \times 2N$ matrix $w(\boldsymbol{k})$ is defined as

$$w_{mn}(\boldsymbol{k}) \equiv \langle u_{m,-\boldsymbol{k}}|\Theta|u_{n,\boldsymbol{k}}\rangle, \quad m,\ n = 1, \cdots, 2N, \tag{2.26}$$

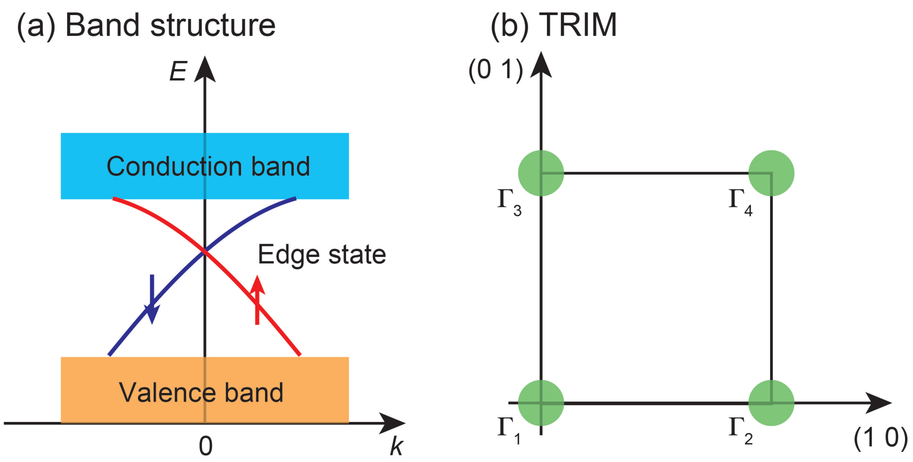

FIGURE 2.10: (a) Schematic drawing of the band structure of 2D TI. (b) TRIM for 2D TI.

where Θ is a time reversal operator. On the other hand, I define time-reversal invariant momenta (TRIM) as $\boldsymbol{k} = -\boldsymbol{k} \pmod{\boldsymbol{G}}$, where $\boldsymbol{G}$ is a reciprocal lattice vector. In 2D system, using the reciprocal lattice unit vectors $\boldsymbol{G}_1$ and $\boldsymbol{G}_2$, there are four TRIM at $\boldsymbol{k} = 0$, $\boldsymbol{G}_1/2$, $\boldsymbol{G}_2/2$, $(\boldsymbol{G}_1 + \boldsymbol{G}_2)/2$, as shown in Fig. 2.10(b). I rewrite these $\boldsymbol{k}$ to $\boldsymbol{k} = \boldsymbol{\Gamma}_i$ (i =1, 2, 3, 4). The Z_2 topological number ν is defined as

$$(-1)^{\nu} = \prod_{i=1}^{4} \frac{\mathrm{Pf}\left(w\left(\boldsymbol{\Gamma}_i\right)\right)}{\sqrt{\det\left(w\left(\boldsymbol{\Gamma}_i\right)\right)}}, \tag{2.27}$$

where Pf and det represent Pfaffian and determinant, respectively. The Z_2 topological number ν takes $\nu = 0$ or $\nu = 1$. When a material shows $\nu = 1$, it is a non-trivial TI. On the other hand, a material that has $\nu = 0$ is a trivial TI, that is to say, not a TI.

Experimentally, for example, Bi thin film [49] and CdTe/HgTe/CdTe quantum well [50–53] are reported as 2D TIs.

Three dimensional topological insulator (3D TI)

Figure 2.11(a) shows a schematic drawing of the band structure of 3D TI. The surface state makes a Dirac cone, which is obtained from a rotation of the band structure of the 2D TI edge state [Fig. 2.10(a)] about the vertical axis.

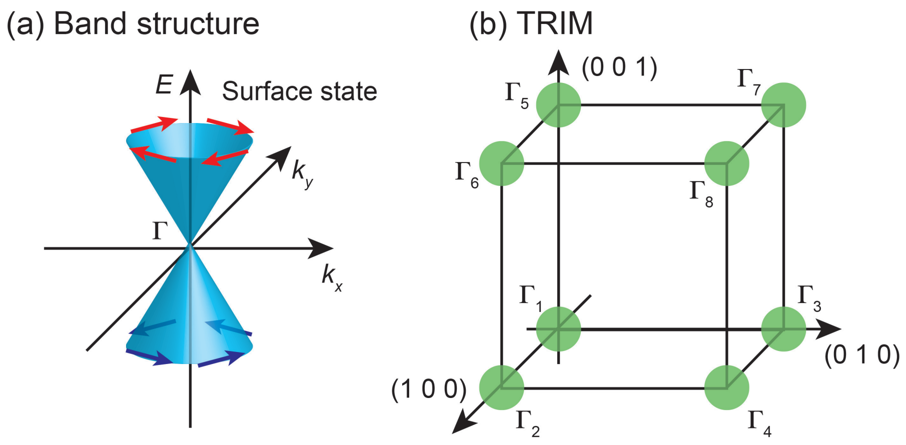

FIGURE 2.11: (a) Schematic drawing of the band structure of 3D TI. (b) TRIM for 3D TI.

In an analogous way to 2D TI, there are eight TRIM in 3D system at $\boldsymbol{k} = \frac{1}{2}(n_1\boldsymbol{G}_1 + n_2\boldsymbol{G}_2 + n_3\boldsymbol{G}_3)$ (n_1, n_2, n_3 = 0, 1), where $\boldsymbol{G}_1$, $\boldsymbol{G}_2$, $\boldsymbol{G}_3$ are the reciprocal lattice unit vectors, as shown in Fig 2.11(b).

For 3D TI, four Z_2 topological numbers, $\nu_0;(\nu_1\nu_2\nu_3)$, are defined as [44, 48]

$$(-1)^{\nu_0} = \prod_{i=1}^{8} \delta_i, \tag{2.28}$$

$$(-1)^{\nu_j} = \prod_{i=(n_1n_2n_3),n_j=1} \delta_i \qquad (j = 1, 2, 3)\,, \tag{2.29}$$

where

$$\delta_i = \prod_{m=1}^{N} \xi_{2m}(\boldsymbol{\Gamma}_i)\,. \tag{2.30}$$

$\xi_{2m}(\boldsymbol{\Gamma}_i)$ is a parity eigenstate (+1 or -1) of the m^{th} state from the lowest energy state at the TRIM $\boldsymbol{k} = \boldsymbol{\Gamma}_i$. It is notable that the parities of $2m-1^{\text{th}}$ and $2m^{\text{th}}$ states are equal ($\xi_{2m} = \xi_{2m-1}$) because of the Kramers degeneracy. The Z_2 topological numbers, ν_0 and ν_j, take 0 or 1, respectively. Furthermore, when $\nu_0 = 1$, the surface states in wherever surface directions make the gapless band structures, thus, this TI is called a strong TI. On the other hand, there is at least one surface state that has a gap when $\nu_0 = 0$, and this type of TI is classified as a weak TI.

Chalcogen compounds are the most famous materials as 3D TI. Figure 2.12(a) shows the crystal structure of Bi_2Se_3 that is one of the chalcogen compounds [54]. It makes a laminate structure composed of Bi and Se, and a unit as a quintuple layer (QL).

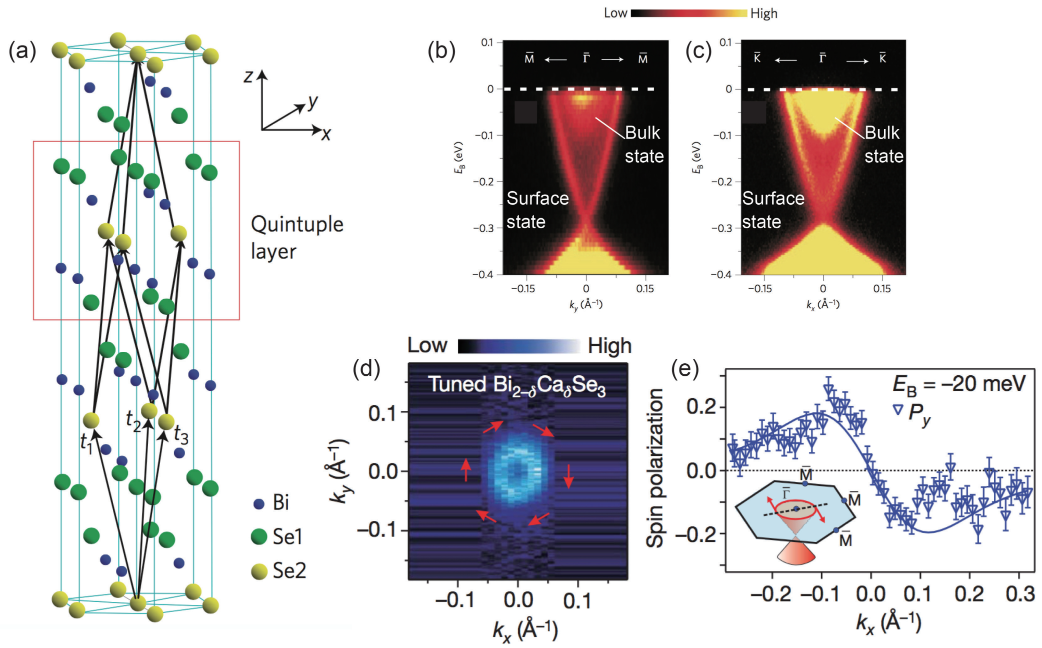

FIGURE 2.12: (a) Schematic drawing of the crystal structure of Bi_2Se_3. t_1, t_2, and t_3 represent three primitive lattice vectors. Bi_2Se_3 makes a unit as a quintuple layer (Se1-Bi1-Se2-Bi1'-Se1'), as indicated by the red square. Taken from Ref. [54]. (b, c) ARPES spectra of $Bi_2Se_3(111)$ near the $\bar{\Gamma}$ along the $\bar{\Gamma}-\bar{M}$ (b) and $\bar{\Gamma}-\bar{K}$ (c) momentum-space cuts. The Fermi energy (E_F) crosses not only the surface state but also the bulk conduction band. Taken from Ref. [55]. (d) ARPES Fermi mapping of $Bi_{2-\delta}Ca_\delta Se_3(111)$. Ca was doped to tune E_F of Bi_2Se_3. The spin directions at E_F are indicated by the arrows. Taken from Ref. [56]. (e) y component of spin polarization along the $\bar{\Gamma}-\bar{M}$ momentum-space cut at the binding energy $E_B = -20$ meV, where the only surface state is included. Schematic drawing of the cut direction is shown in the inset. Taken from Ref. [56].

Figures 2.12(b) and (c) show the results of angle-resolved photoelectron spectroscopy (ARPES) for Bi_2Se_3 [55], and it was reported that its surface state shapes a Dirac cone, as shown in Fig. 2.11(a). Furthermore, spin-resolved ARPES showed the helical spin polarization of the surface state of Bi_2Se_3 that is the fundamental feature of TI, as shown in Figs. 2.12(d) and (e) [56].

Chapter 3

Experimental methods

3.1 Light source

3.1.1 Principle of synchrotron radiation (SR)

Synchrotron radiation (SR) [57, 58] is an electromagnetic radiation emitted when a high-energy electron is accelerated radially, ordinarily, the electron is forced to travel in a curved path by a magnetic field, as shown in Fig. 3.1. Comparing with other light sources that enable us to use a limited energy range, SR can cover a broad range, from microwaves to X-rays and gamma rays. Figure 3.2 shows a classification of the electromagnetic radiation based on its energy (wavelength). Furthermore, SR has a high directionality due to the relativistic effect, as shown in Fig. 3.1. Using a velocity of an electron, v, a relative velocity is defined as $\beta = v/c$, where c is a speed of light in

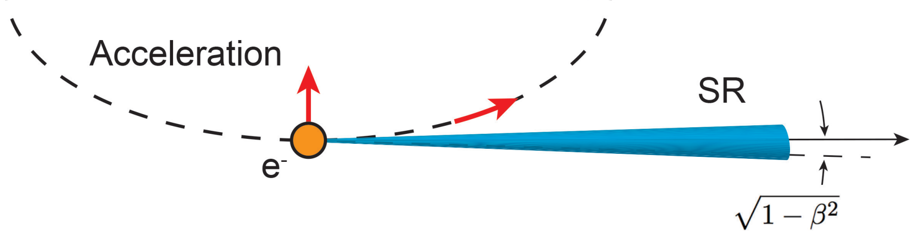

FIGURE 3.1: Schematic drawing of the emission of SR with an angle distribution of the radiation power.

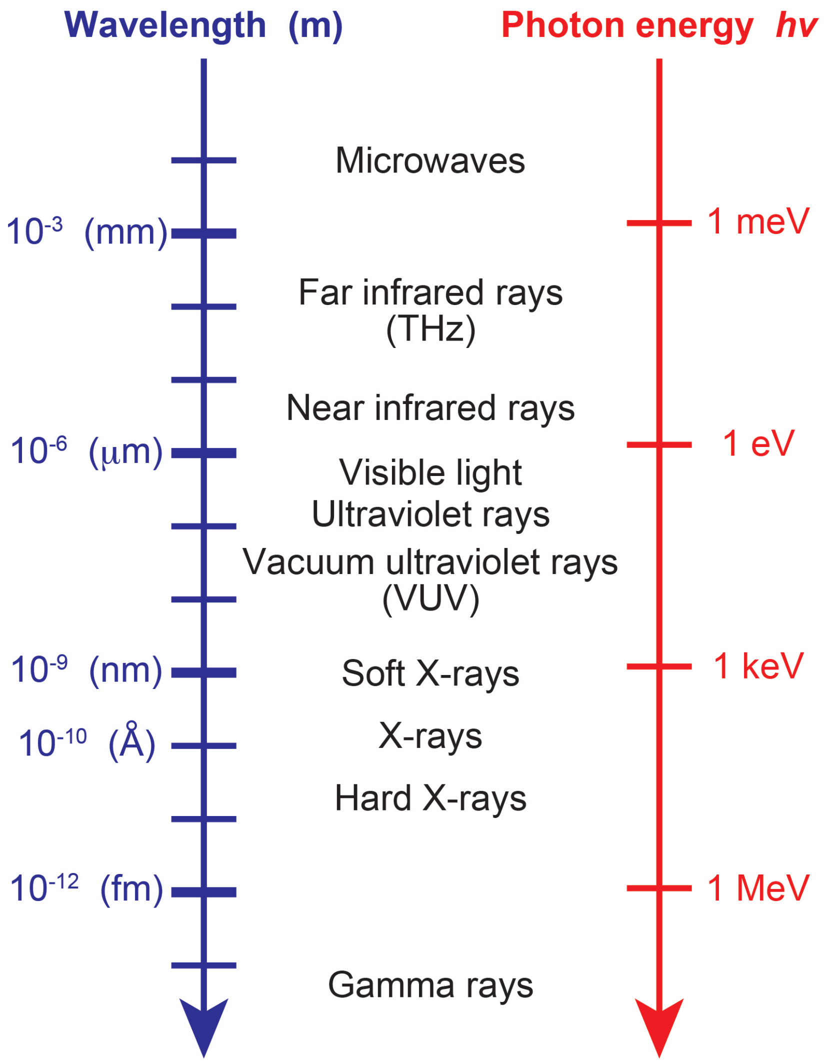

FIGURE 3.2: Classification of the electromagnetic radiation based on its wavelength (left axis) and energy (right axis).

vacuum. I shall define γ as

$$\gamma = \frac{1}{\sqrt{1-\beta^2}} = 1957E \quad [\mathrm{GeV}]\,, \tag{3.1}$$

where E represents the electron's energy. Hence, an expectation of Ψ, which is a half of an angle of SR's space distribution, is calculated as

$$\langle \Psi^2 \rangle^{1/2} \approx \frac{1}{\gamma} = \sqrt{1-\beta^2}. \tag{3.2}$$

A photon number (n) distribution of SR, called the brightness, is expressed as functions of a wavelength (λ) and a solid angle from the light source (Ω)

$$\begin{aligned}
&\frac{d^3 n}{dt d\Omega d\lambda/\lambda} \ \left[\mathrm{photons/sec/mrad^2/0.1\%b.w./mA}\right] \\
&= 3.46 \times 10^3 \gamma^3 \left(\frac{\lambda_c}{\lambda}\right)^2 \left\{1 + (\gamma\Psi)^2\right\}^2 \left\{K_{2/3}^2(\xi) + \frac{(\gamma\Psi)^2}{1+(\gamma\Psi)^2} K_{1/3}^2(\xi)\right\}, \qquad (3.3)
\end{aligned}$$

where $K_{2/3}$ and $K_{1/3}$ are the modified Bessel functions of the second kind, and ξ is defined as

$$\xi = \lambda_c \left\{1 + (\gamma\Psi)^2\right\}^{3/2}. \qquad (3.4)$$

λ_c and ε_c are the critical wavelength and the critical energy, respectively, and defined as

$$\lambda_c \ [\text{Å}] = 5.59 \frac{\rho \ [\mathrm{m}]}{E^3 \ [\mathrm{GeV}]} = \frac{18.6}{E^2 \ [\mathrm{GeV}] \, B \ [\mathrm{tesla}]}, \qquad (3.5)$$

$$\varepsilon_c \ [\mathrm{keV}] = \frac{12.4}{\lambda_c \ [\text{Å}]} = \frac{2.22 E^3 \ [\mathrm{GeV}]}{\rho \ [\mathrm{m}]}, \qquad (3.6)$$

where ρ and B represent a radius of the electron circular trajectory and a strength of the magnetic field, respectively. λ_c and ε_c are also defined where the total radiation power is divided in half, and they are near the peaks of spectra. The integrated value of the brightness with respect to Ψ is called the photon flux. On the other hand, the divided value of the brightness by the size of light source is defined as the brilliance.

The first and second terms in the last bracket in Eq. (3.3) express the parallel and perpendicular components of the electric field to the plane of trajectory (I_P and I_N), respectively. Using I_P and I_N, degrees of linear and circular polarization (P_L and P_C) are expressed as

$$P_L = \frac{I_P - I_N}{I_P + I_N} = \frac{K_{2/3}^2(\xi) - \frac{(\gamma\Psi)^2}{1+(\gamma\Psi)^2} K_{1/3}^2(\xi)}{K_{2/3}^2(\xi) + \frac{(\gamma\Psi)^2}{1+(\gamma\Psi)^2} K_{1/3}^2(\xi)}, \qquad (3.7)$$

$$P_C = \pm \frac{\sqrt{I_P I_N}}{I_P + I_N}, \qquad (3.8)$$

where + (-) corresponds when $\Psi > 0$ ($\Psi < 0$). When $\Psi = 0$, $P_L = 1$ and $P_C = 0$. Furthermore, P_L decreases, while P_C increases with increasing of $|\Psi|$.

In this thesis, I shall focus on the vacuum ultraviolet (VUV) and soft X-ray energy region. Their ranges are defined around $\lambda \sim 10$ nm (about 10 eV) for VUV, and 1 Å $\sim$ 10 nm order (1 keV$\sim$10 eV order) for soft X-ray, as shown in Fig. 3.2. These energy ranges cover a lot of absorption edges, and a strong interaction between light and materials is observed there. Therefore, it enables us to do many kinds of measurements with element-selectivity and a resonant enhancement.

3.1.2 Undulators

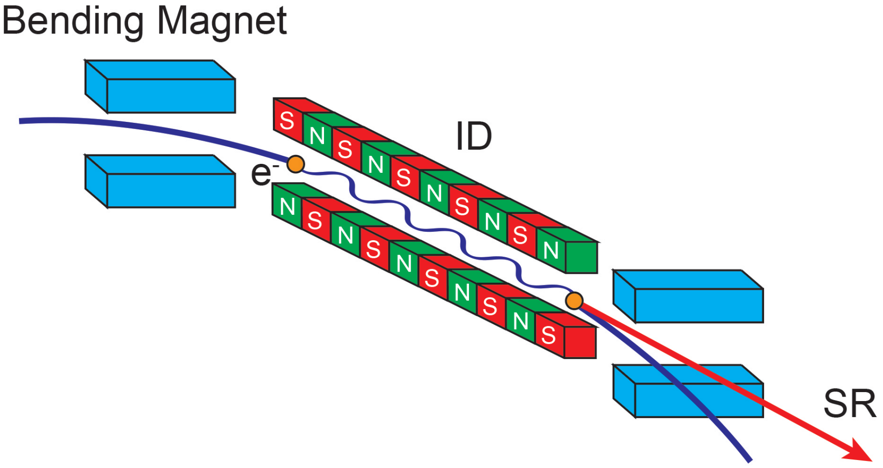

FIGURE 3.3: Schematic drawing of an insertion device (ID). Based on Ref. [59].

An insertion device (ID) is a light source of SR [59]. It can generate much more intense SR than that obtained by only bending magnets, as described above. The ID consists of two magnet lines where two polarized magnets (N and S) line up alternately, and N and S magnets face each other vertically, as shown in Fig. 3.3. In a SR ring, the ID is inserted in the straight section between bending magnets. High-energy electrons pass between the two magnet lines and take a sinusoidally serpentine motion derived from the magnetic period. Hence, SR is emitted with high-brilliance.

A parameter K is defined as

$$K = \frac{eB\lambda_0}{2\pi mc} = 0.934B \ [\mathrm{tesla}] \, \lambda_0 \ [\mathrm{cm}] \,, \tag{3.9}$$

where e and m are the elementary charge and the electron mass, respectively. B is a maximum value of the magnetic field in the ID, and λ_0 is a period length of the magnetic field. When $K \gg 1$, the ID is called a wiggler and SR is emitted only near peaks of the electron sinusoidally motion. Another type of ID is called an undulator when $K \leq 1$. The undulator can generate SR without a break in the electron motion, and its beam size and angular spread are much smaller than those generated from the wiggler. This feature is suitable for the SR ring that has a low-emittance electron beam [59].

From here, I focus on the undulator. The undulator with a weak magnetic field ($K \ll 1$) can generate a quasi-monochromatic light where the fundamental wave is dominant. When $K \approx 1$, not only the fundamental wave but also odd-order harmonic waves can be generated. A wavelength of k order harmonic wave is expressed as

$$\lambda_k = \frac{\lambda_0}{2k\gamma^2}\left(1 + \frac{K^2}{2} + \gamma^2\theta^2\right), \tag{3.10}$$

where θ is an angle between the beam direction and the straight line of the undulator. Its brightness is calculated as

$$\begin{aligned} &\frac{d^3n}{dtd\Omega d\omega} \ \left[\mathrm{photons/sec/mrad^2/0.1\%b.w./mA}\right] \\ &= 4.555 \times 10^4 \gamma^2 N^2 \xi_k^2 K^2 \left\{ J_{(k-1)/2}\left(\frac{\xi_k K^2}{4}\right) - J_{(k+1)/2}\left(\frac{\xi_k K^2}{4}\right)\right\}^2, \end{aligned} \tag{3.11}$$

where $\xi_k = k/\left(1 + K^2/2\right)$, N is a periodic number of the undulator, ω is a frequency, and J_k is the k order Bessel function.

Planar undulators, as shown in Fig. 3.3, generate a magnetic field vertically or horizontally. When an electron passes the undulator with a vertical (horizontal) magnetic field, horizontal (vertical) polarized light is emitted. To get circular polarized light, especially, the VUV $\sim$ soft X-ray region, a helical undulator is used (in the hard X-ray region, wavelength plates are used). Figure 3.4 shows a schematic drawing of the helical undulator used at SPring-8 [59]. In the helical undulator, the electron trajectory shapes a helix and it generates circular polarized light. Moreover, SR emitted from the helical undulator includes only the fundamental wave on the straight line axis. This type of undulator consists of three magnet lines at the top and bottom. The vertical magnetic field can be generated by the central magnet line, while the lines at both sides generate the horizontal magnetic field. Moreover, left-circular polarized light (LCP) and right-circular polarized light (RCP) can be switched by shifting the central magnet line, which is called phasing.

To generate linear polarized soft X-ray when the electron energy is very high, such as SPring-8, a figure-8 undulator is employed [59, 60]. Figure 3.5 shows a schematic drawing of the figure-8 undulator. The electron trajectory resembles the figure of eight (8) in the figure-8 undulator, as shown in Fig. 3.5 (upper right) and horizontal polarized light is generated by this type of undulator. In order to create the figure-8 undulator,

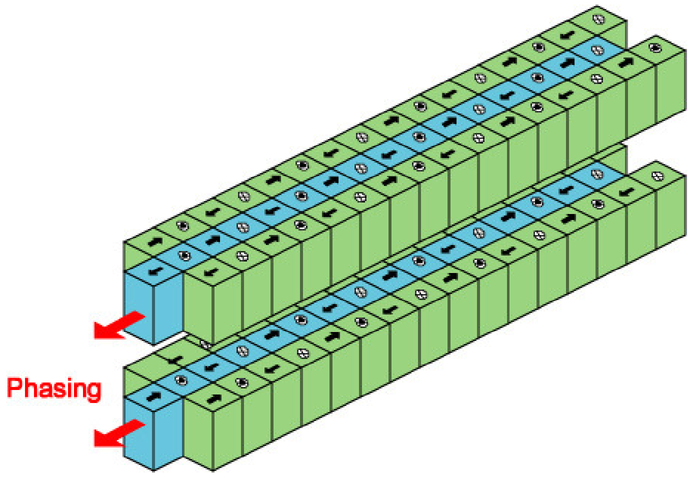

Figure 3.4: Schematic drawing of the helical undulator used at SPring-8. LCP or RCP can be switched by phasing. Taken from Ref. [59].

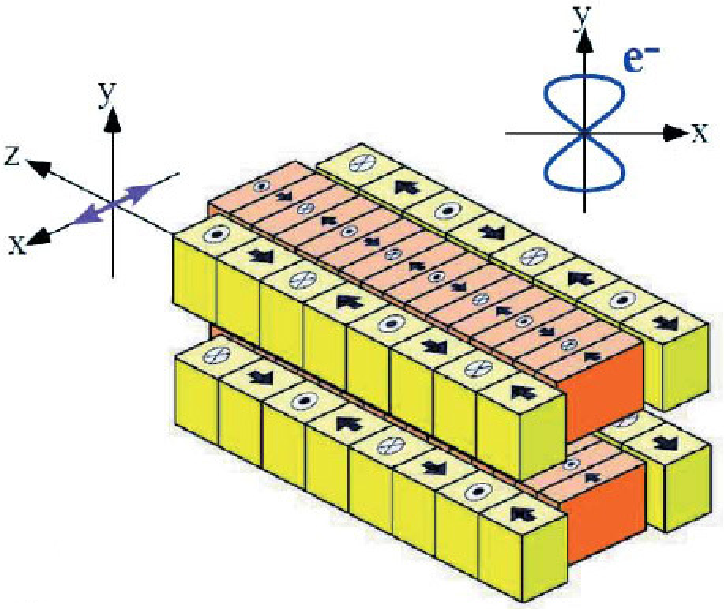

Figure 3.5: Schematic drawing of the figure-8 undulator. Upper right figure shows the trajectory of the electron in the figure-8 undulator. Taken from Ref. [60].

the periodic length of the magnet lines at both sides in the helical undulator (Fig. 3.4) is slightly changed to doubling along the z-axis (the straight direction of the undulator), as shown in Fig. 3.5.

3.2 Measurement

3.2.1 Photoelectron spectroscopy (PES)

Photoelectron spectroscopy (PES) [61] is one of the powerful methods to measure an electron state in a solid. This technique detects a kinetic energy of a photoelectron generated by the photoelectric effect investigated by A. Einstein [62]. The kinetic energy of the photoelectron (E_k) in vacuum is expressed as

$$E_\mathrm{k} = h\nu - E_\mathrm{B} - \phi, \tag{3.12}$$

where $h\nu$ is a photon energy injected to the solid, E_B is a binding energy of the electron in the solid respect to the Fermi energy (E_F). The work function, ϕ, is normally $\phi = 4 \sim 5$ eV. Figure 3.6 shows the principle of the PES process. From the Fermi's Golden Rule, the transition probability (ω) of the electron from the initial state ψ_i with the energy E_i to the final state ψ_f with the energy E_f expressed as

$$\omega \propto \frac{2\pi}{\hbar} | \langle \psi_f | \mathit{\Delta} | \psi_i \rangle |^2 \delta \left(E_f - E_i - h\nu \right), \tag{3.13}$$

$$\mathit{\Delta} = \frac{e}{2mc} \left(\boldsymbol{A} \cdot \boldsymbol{p} + \boldsymbol{p} \cdot \boldsymbol{A} \right) - e\phi_s + \frac{e^2}{2mc^2} \boldsymbol{A} \cdot \boldsymbol{A}, \tag{3.14}$$

where $\boldsymbol{A}$ and ϕ_s are the vector and scalar potentials and $\boldsymbol{p}$ represents the momentum operator $\boldsymbol{p} = i\hbar\boldsymbol{\nabla}$. m is the free electron mass. The commutation relation in Eq. (3.14) is calculated as $\boldsymbol{A} \cdot \boldsymbol{p} + \boldsymbol{p} \cdot \boldsymbol{A} = 2\boldsymbol{A} \cdot \boldsymbol{p} + i\hbar \left(\boldsymbol{\nabla} \cdot \boldsymbol{A} \right)$. If the gauge $\phi_s = 0$ is chosen, the two photon emission term $\boldsymbol{A} \cdot \boldsymbol{A}$ can be neglected, and one assumes that $\boldsymbol{\nabla} \cdot \boldsymbol{A} = 0$ because of the translational invariance in the solid, Eq. (3.14) can be rewritten as

$$\mathit{\Delta} = \frac{e}{mc} \boldsymbol{A} \cdot \boldsymbol{p}. \tag{3.15}$$

Normally, because the wavelength of the incident light is large compared to the atomic distances, $\boldsymbol{A}$ can be taken as constant $\boldsymbol{A} = A_0$. Therefore, the bracket in Eq. (3.13) can be calculated as

$$\langle \psi_f | \mathit{\Delta} | \psi_i \rangle \propto \langle \psi_f | \boldsymbol{A} \cdot \boldsymbol{p} | \psi_i \rangle \propto \langle \psi_f | \boldsymbol{A} \boldsymbol{\nabla} \cdot V | \psi_i \rangle \propto \langle \psi_f | \boldsymbol{A} \cdot \boldsymbol{r} | \psi_i \rangle = A_0 \langle \psi_f | \boldsymbol{r} | \psi_i \rangle, \tag{3.16}$$

where V is the electron-electron interaction.

Here, it is assumed that a system has N electrons and an electron is photoexcited from the initial state ϕ_i to the final state (a free electron) ϕ_{f,E_k} with energy E_k. Furthermore,

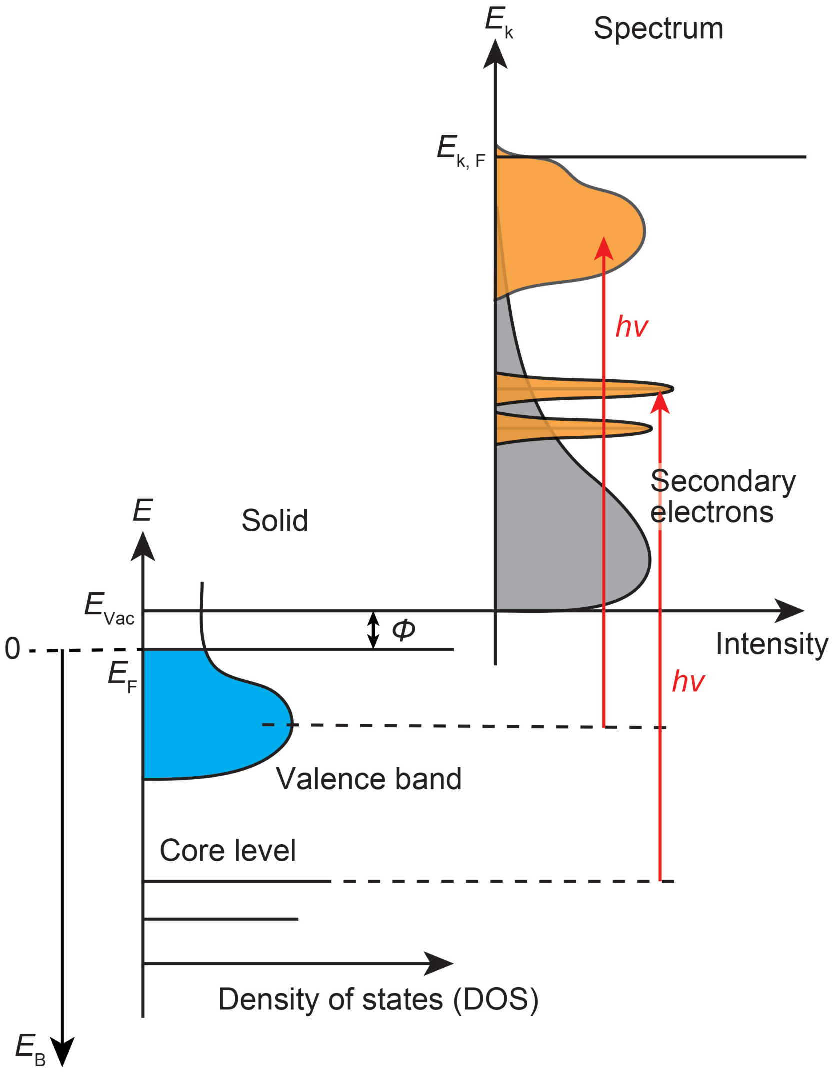

FIGURE 3.6: Schematic drawing of the PES process [61]. E_{Vac} is the vacuum energy level.

the remaining $N-1$ electrons change from the initial state $\psi_i\,(N-1)$ to the final state $\psi_{f,s}\,(N-1)$ that has s excited states with energy $E_s\,(N-1)$. s is used as the number of states and the running index. In this situation, Eq. (3.16) is rewritten as

$$\langle\psi_f|\boldsymbol{r}|\psi_i\rangle = \langle\phi_{f,E_{\mathrm{k}}}|\boldsymbol{r}|\phi_i\rangle \sum_s c_s, \tag{3.17}$$

with

$$c_s = \langle\psi_{f,s}\,(N-1)\,|\psi_i\,(N-1)\rangle\,. \tag{3.18}$$

$|c_s|^2$ is the probability that the removal of a photoelectron from the initial state ϕ_i of the

N-electron ground state leaves the system in the excited state s of the $N-1$-electron system. The intensity of PES (I) in this situation is expressed as

$$I \propto \sum_{s,i} |\left\langle \phi_{f,E_\mathrm{k}} | \boldsymbol{r} | \phi_i \right\rangle|^2 |c_s|^2 \delta\left(E_\mathrm{k} + E_s\left(N-1\right) - E_0\left(N\right) - h\nu\right) \delta\left(E - E_f + \phi\right) f(E,T), \tag{3.19}$$

where $E_0\left(N\right)$ is the ground state energy of the N-electron system and $f(E,T)$ is the Fermi distribution function. Moreover, the spectral function of an electron with energy E and momentum $\boldsymbol{k}$ is defined as

$$A\left(\boldsymbol{k}, E\right) = \sum_s |c_s|^2. \tag{3.20}$$

$A\left(\boldsymbol{k}, E\right)$ and the one-electron Green's function $G\left(\boldsymbol{k}, E\right)$ are related by the equation

$$A\left(\boldsymbol{k}, E\right) = \frac{1}{\pi}\left[\mathrm{Im}G\left(\boldsymbol{k}, E\right)\right], \tag{3.21}$$

where $G\left(\boldsymbol{k}, E\right)$ is expressed with the self-energy $\varSigma\left(\boldsymbol{k}, E\right)$ as

$$G\left(\boldsymbol{k}, E\right) = \frac{1}{E - E^0\left(\boldsymbol{k}\right) - \varSigma\left(\boldsymbol{k}, E\right)}, \tag{3.22}$$

with $E^0\left(\boldsymbol{k}\right) = \hbar^2 \boldsymbol{k}^2/(2m)$. Eventually, $A\left(\boldsymbol{k}, E\right)$ is expressed as

$$A\left(\boldsymbol{k}, E\right) = \frac{1}{\pi}\frac{\mathrm{Im}\varSigma}{\left(E - E^0\left(\boldsymbol{k}\right) - \mathrm{Re}\varSigma\right)^2 + \left(\mathrm{Im}\varSigma\right)^2}. \tag{3.23}$$

Three step model

As mentioned above, the photoelectric effect in the solid can be described by one step transition in the N-electron system (the one step model). Nevertheless, the PES process can be divided into three steps (the three step model) and it can describe the process more successfully than the one step model. Figure 3.7 shows a schematic drawing of the three step model of the PES process.

In the first step, electrons in the solid are photoexcited by the incident light with energy $h\nu$. Its detail has been already described above.

In the second step, the photoexcited electrons are scattered and transported to the surface. Not only the electrons whose energies are conserved by the elastic scattering but also the secondary electrons which lose their energies are generated by the inelastic scattering. The average distance where an electron does not lose its energy in solids

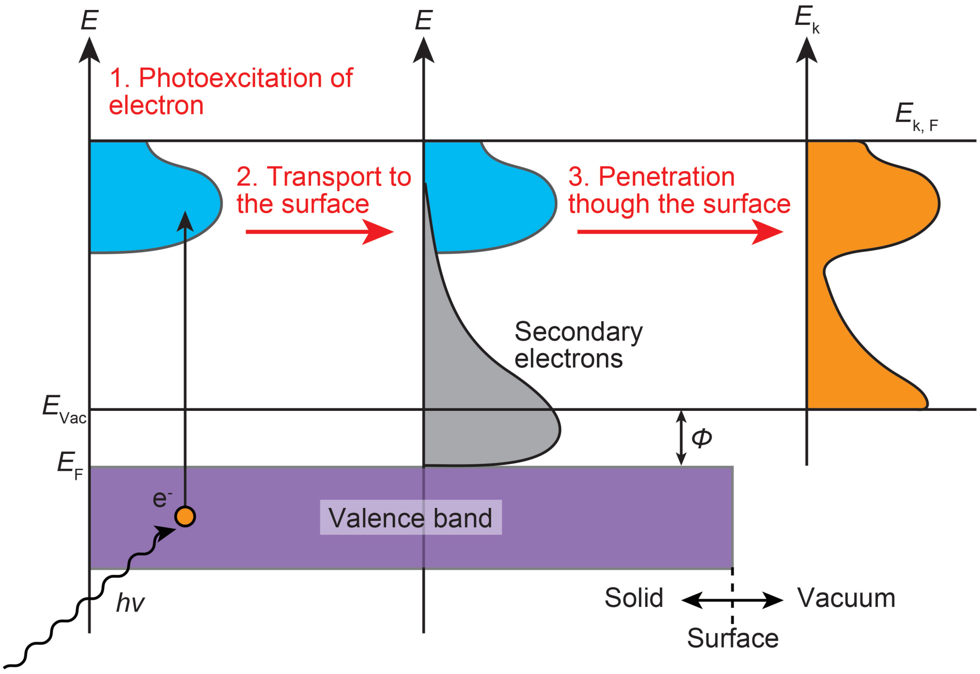

FIGURE 3.7: Schematic drawing of the three step model of the PES process [61]. The process is divided into (1) photoexcitation of electrons, (2) transport of the photoelectrons to the surface, and (3) penetration through the surface. The horizontal axes denote the DOS.

is called the mean-free path and depends on the kinetic energy of electron, as shown in Fig. 3.8. As one can see, the relation between the mean-free path and the kinetic energy of electron is independent on elements of solids, so-called the universal curve. When the incident light with $h\nu = 50 \sim 80$ eV is used for PES, the electrons that escape from the solid in ~ 5 Å depth can be detected, therefore, it is surface sensitive. On the other hand, in the other photon energy regions, one can operate a relatively bulk sensitive PES.

In the final step, photoelectrons penetrate to the vacuum through the surface. The photoelectrons which have larger energies than the work function ϕ can escape from the solid and be detected.

Angle-resolved photoelectron spectroscopy (ARPES)

Angle-resolved photoelectron spectroscopy (ARPES) is the only technique that enables us to determine band structures of materials. In ARPES, not only the kinetic energy of the photoelectron but also its momentum can be detected by an analyzer,

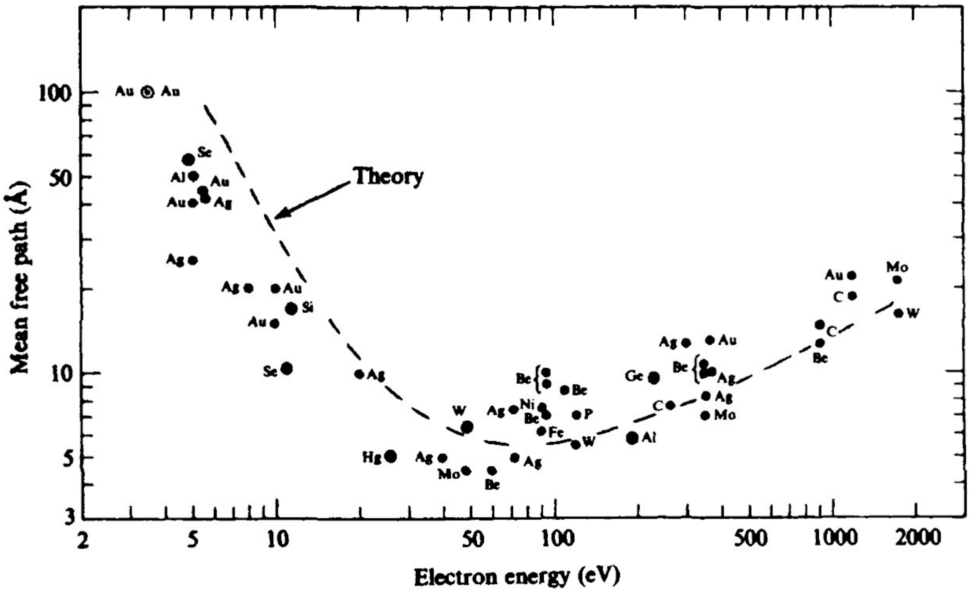

Figure 3.8: Universal curve of electrons in solids taken from Ref. [63]. The dashed line represents the theoretical curve independent of elements.

such as a hemispherical PES analyzer, as shown in Fig. 3.9. Because the photon energy is normally low in ARPES, the wave number of the incident photon can be neglected, and the momentum of the photoelectron is conserved before and after the photoexcitation except for the reciprocal lattice vector ($\boldsymbol{G}$) of the solid. The momenta of the initial state ($\boldsymbol{K}_i$) and the final state ($\boldsymbol{K}_f$) have a relation as

$$\boldsymbol{K}_f = \boldsymbol{K}_i + \boldsymbol{G}. \tag{3.24}$$

When the photoelectron is emitted from the solid to the vacuum, the momentum parallel to the surface ($\boldsymbol{K}_{f//}$) is conserved, while the momentum perpendicular to the surface ($\boldsymbol{K}_{f\perp}$) is not done due to the inner potential (V_0), as shown in Fig. 3.9. The momentum parallel to the surface of the emitted photoelectron ($\boldsymbol{k}_{f//}$) is expressed as

$$\boldsymbol{k}_{f//} = \boldsymbol{K}_{f//} = \boldsymbol{K}_{i//}. \tag{3.25}$$

Using the polar emission angle θ, E_k, and Eq. (3.12), $k_{f//}$ is calculated by

$$\begin{aligned} k_{f//}\,[\text{Å}^{-1}] &= \frac{\sqrt{2m}}{\hbar}\sqrt{E_\mathrm{k}}\sin\theta & (3.26)\\ &= 0.5123\sqrt{h\nu - E_\mathrm{B} - \phi\,[\mathrm{eV}]}\sin\theta, & (3.27)\end{aligned}$$

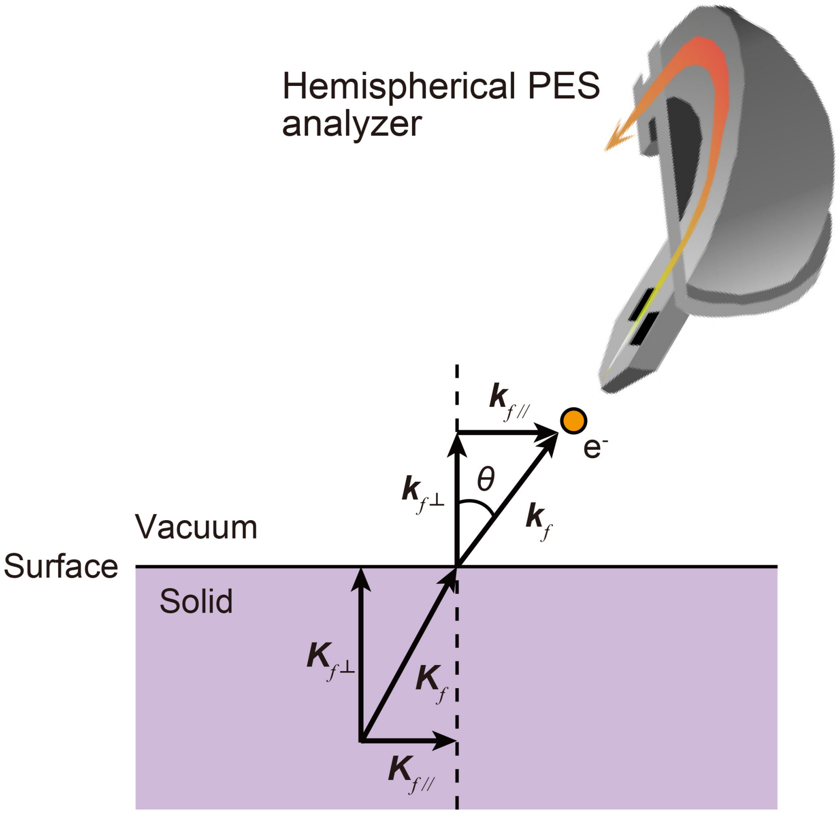

FIGURE 3.9: Schematic drawing of the emission of a photoelectron from a solid to the vacuum and its detection by a hemispherical PES analyzer.

therefore, $\boldsymbol{K}_{i//}$ is given by

$$\boldsymbol{K}_{i//}\left[\text{Å}^{-1}\right] = 0.5123\sqrt{h\nu - E_{\mathrm{B}} - \phi\,[\mathrm{eV}]}\,\sin\theta. \tag{3.28}$$

On the other hand, $\boldsymbol{K}_{i\perp}$ is calculated by

$$\boldsymbol{K}_{i\perp}\left[\text{Å}^{-1}\right] = 0.5123\sqrt{(h\nu - E_{\mathrm{B}} - \phi)\cos^2\theta + V_0\,[\mathrm{eV}]}. \tag{3.29}$$

3.2.2 X-ray magnetic circular dichroism (XMCD) measurement

X-ray absorption spectroscopy (XAS)

X-ray absorption spectroscopy (XAS) is a measurement of photo-absorption by the excitation of a core electron into unoccupied states depending on photon energy. Its intensity is written as

$$I\left(h\nu\right)=\sum_{f}\left|\left\langle f|T|i\right\rangle\right|^{2}\delta\left(E_{i}-E_{f}-h\nu\right), \tag{3.30}$$

where T is the dipole transition operator. i (f) and $E_{i(f)}$ represent the initial (final) state and its energy of the optical transition, respectively.

To measure XAS spectrum in the hard X-ray energy region, the transmission mode, where a ratio of the transmitted X-ray is obtained by the measurement of the X-ray intensity at in front of and behind the sample, is widely used. On the other hand, in the soft X-ray energy region, because of a strong interaction between light and the sample, it is difficult to measure XAS spectrum by the transmission mode, therefore, the yield mode is used. There are two types of the yield mode; one is the electron yield mode and the other is the fluorescence yield mode. The electron yield mode is a method detecting the amount of the electrons emitted by the incident soft X-ray, while the fluorescence X-ray emitted from the sample is measured in the fluorescence yield mode. Furthermore, the electron yield mode can be classified into the Auger electron yield (AEY), the partial electron yield (PEY), and the total electron yield (TEY) modes. The AEY method measures the amount of the Auger electrons. All escaping electrons excited by the soft X-ray are detected in the TEY mode, while the PEY method selects the energy of detected electrons. Since XAS spectrum can be measured simply by measuring the current that flows in the sample (sample current) in the TEY mode, this yield mode is most widely used and a convenient technique. Figure 3.10 shows a schematic drawing of the TEY and total fluorescence yield (TFY) methods that were adopted in our experiments. The probing depths of the electron yield and the fluorescence yield modes are about 5 $\sim$ 10 nm and 10 $\sim$ 100 nm depending on the electron escape depth and the photon mean-free path, respectively [17]. Therefore, the electron yield mode is surface sensitive, while the fluorescence yield mode is bulk sensitive.

X-ray magnetic circular dichroism (XMCD) spectroscopy

X-ray magnetic circular dichroism (X-ray MCD, XMCD) spectroscopy [64, 65] is one of the most leading methods to get the magnetic information. XMCD spectrum is derived from the difference between the two absorption spectra obtained by circular polarized light of opposite helicities, as shown in Fig 3.10. Using absorption edges, the merit of this measurement is that one can use element-selectivity and a resonant

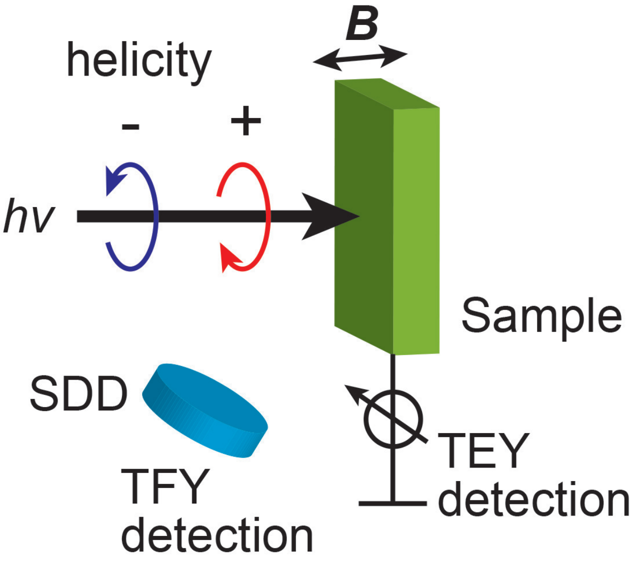

FIGURE 3.10: Schematic drawing of a XMCD experimental set up. The TEY method measures the sample current. A silicon drift detector (SDD) was used for the TFY mode in our experiments.

enhancement. Moreover, one can obtain the values of the spin and orbital magnetic moments by combining XMCD spectroscopy and the sum rules [5–7]. According to the sum rules, their magnetic moments in units of μ_B/atom (m_{spin} and m_{orb}) are calculated by

$$m_{\text{orb}} = -\frac{4\int_{L_3+L_2}(\mu_+ - \mu_-)\,d\omega}{3\int_{L_3+L_2}(\mu_+ + \mu_-)\,d\omega}(10 - n_{3d})\,, \tag{3.31}$$

$$m_{\text{spin}} = -\frac{6\int_{L_3}(\mu_+ - \mu_-)\,d\omega - 4\int_{L_3+L_2}(\mu_+ - \mu_-)\,d\omega}{\int_{L_3+L_2}(\mu_+ + \mu_-)\,d\omega}(10 - n_{3d})\left(1 + \frac{7\langle T_z\rangle}{2\langle S_z\rangle}\right)^{-1}, \tag{3.32}$$

where n_{3d} is the $3d$ electron occupation number of the specific transition metal atom. The L_3 and L_2 represent the integration energy range, around the L_3- and L_2-edges, respectively. $\langle T_z\rangle$ is the expectation value of the magnetic dipole operator and $\langle S_z\rangle$ is equal to half of m_{spin} in Hartree atomic units. $\mu_\pm$ are the spectra obtained by the helicity ±, respectively. C. T. Chen *et al.* made the first report of the accurate determination of m_{spin} and m_{orb} obtained from the XMCD spectra and the sum rules [7]. The integrated values of the MCD spectrum, p and q, are defined as

$$p = \int_{L_3}(\mu_+ - \mu_-)\,d\omega, \tag{3.33}$$

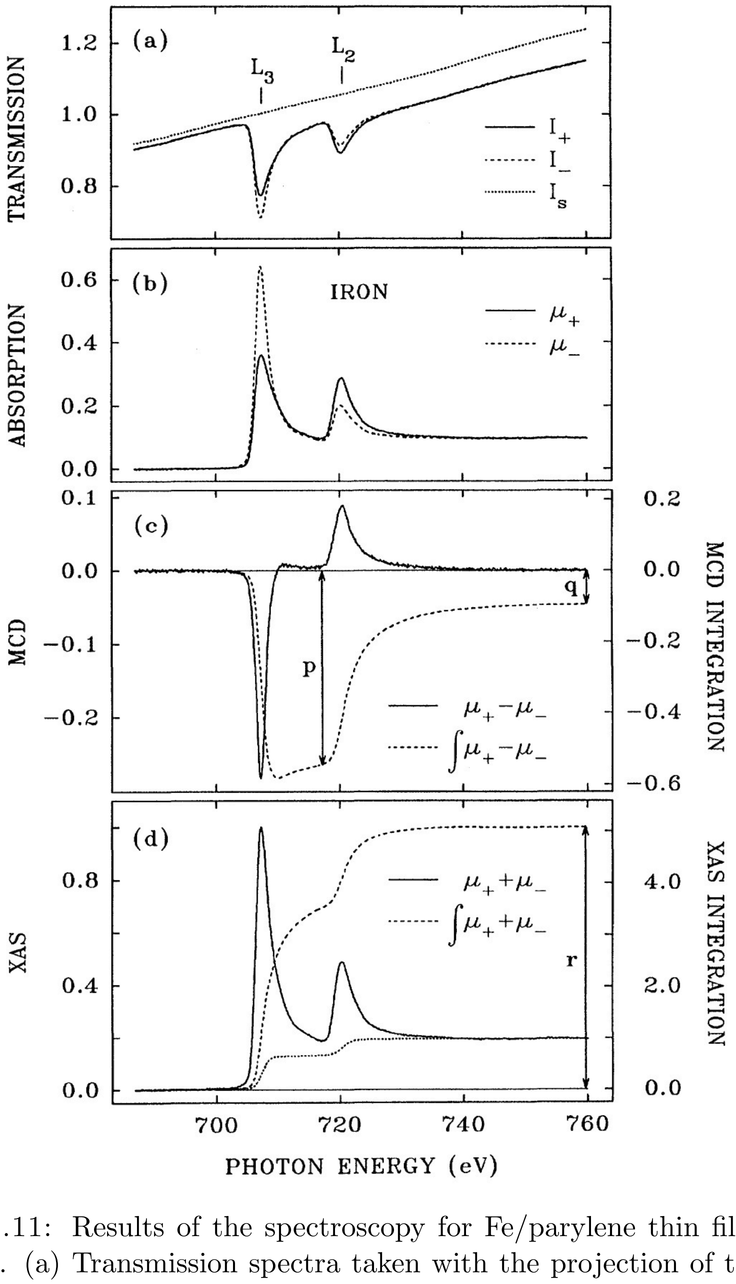

FIGURE 3.11: Results of the spectroscopy for Fe/parylene thin films at the Fe L-edge. (a) Transmission spectra taken with the projection of the spin of incident photons parallel (I_+, solid curve) and antiparallel (I_-, dashed curve) to the spin of the Fe $3d$ majority electrons (I_+ and I_- are equal to the spectra obtained by the helicity + and − when the direction of magnetization is fixed, respectively). I_s represents the spectrum of the parylene substrates alone. (b) Absorption spectra obtained from I_+ and I_-. (c) MCD spectrum (solid line) and its integration (dashed line). (d) Summed XAS spectrum (solid line) and its integration (dashed line). The dotted line represents the two-step-like function for edge-jump removal before the integration. Taken from Ref. [7].

$$q = \int_{L_3+L_2} (\mu_+ - \mu_-)\, d\omega. \tag{3.34}$$

r is also the integrated value of the XAS spectrum after removing the two-step-like function for edge-jump, as shown in Fig. 3.11(d),

$$r = \int_{L_3+L_2} (\mu_+ + \mu_-)\, d\omega. \tag{3.35}$$

From Eqs. (3.31)–(3.35), when the value of $\langle T_z \rangle / \langle S_z \rangle$ is negligible, the $m_{\rm orb}$ to $m_{\rm spin}$ ratio can be calculated as

$$\frac{m_{\rm orb}}{m_{\rm spin}} = \frac{2q}{9p - 6q}. \tag{3.36}$$

C. T. Chen *et al.* measured the XMCD spectra of Fe and Co thin films, and determined their ratios $m_{\rm orb}/m_{\rm spin}$ and the individual values of $m_{\rm orb}$ and $m_{\rm spin}$, as shown in Table 3.1 [7]. It is notable that they used the theoretical values for n_{3d}. These values are in good agreement with those determined by the theoretical calculations or the gyromagnetic ratio measurements.

TABLE 3.1: Ratios $m_{\rm orb}/m_{\rm spin}$ and individual values of $m_{\rm orb}$ and $m_{\rm spin}$ for Fe (body-centered cubic, bcc) and Co (hexagonal close-packed, hcp) obtained from the XMCD spectra and the sum rules. Taken from Ref. [7].

	Fe (bcc)	Co (hcp)
$m_{\rm orb}/m_{\rm spin}$	0.043	0.095
$m_{\rm orb}$	0.085	0.154
$m_{\rm spin}$	1.98	1.62

3.2.3 Magneto-optical Kerr effect (MOKE) measurement

Magneto-optical Kerr effect (MOKE) measurement is a powerful technique to extract the magnetic information. While polarizers and a 1/4 wavelength plate are normally used to observe the Kerr rotation angle ($\theta_{\rm K}$) and the ellipticity ($\varepsilon_{\rm K}$) with visible light, they can be determined by the rotating-analyzer ellipsometry (RAE) [28] in the VUV ~ soft X-ray energy region. Figure 3.12(a) shows a set up of the resonant longitudinal MOKE (L-MOKE) measurement with the RAE. The RAE unit is composed of a multilayer mirror as an analyzer, and a detector. The elements and layer thicknesses of the multilayer mirror are optimized to reflect the light that has the incident photon energy. In this thesis, we used the multilayer mirror made of W/B$_4$C with N = 100 periods for periodic distances of d = 1.19 nm for the Fe L-edge (NTT-AT Corporation), and

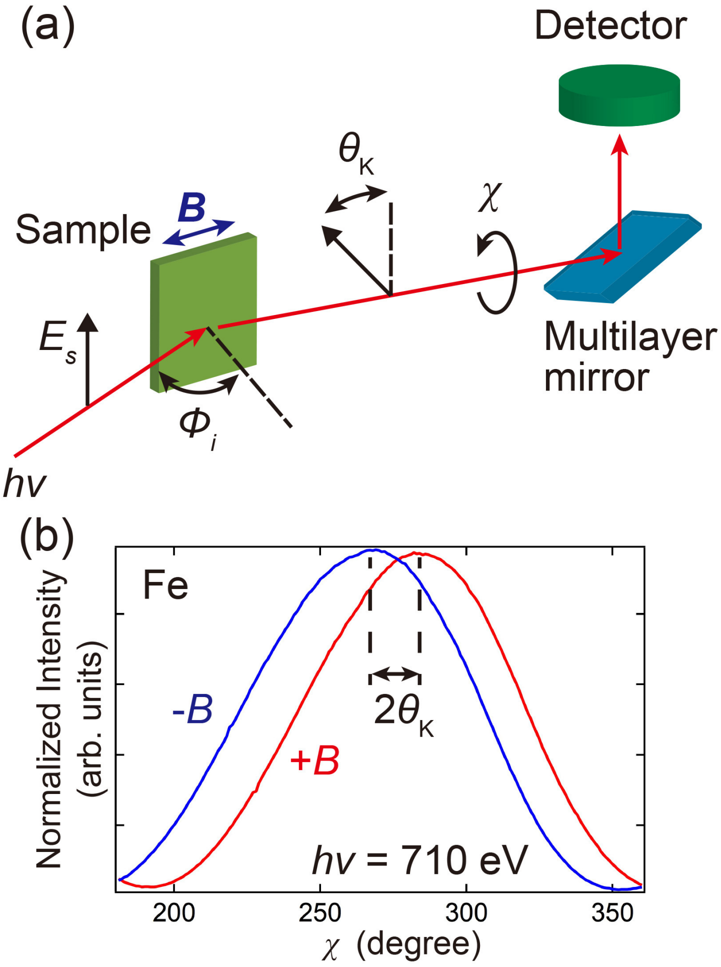

FIGURE 3.12: (a) Set up of the L-MOKE measurement with the RAE. The RAE unit comprises by a multilayer mirror and a detector. (b) Typical results of the intensity variation with rotation angle, χ, for an Fe film taken at $h\nu = 710$ eV. The red and blue solid lines represent the spectra obtained when the magnetic fields were $+0.3$ T ($+B$) and -0.3 T ($-B$), respectively. θ_{K} can be determined from $2\theta_{\mathrm{K}}^{s} = \theta\,(-B) - \theta\,(+B)$ for the s-wave, $2\theta_{\mathrm{K}}^{p} = \theta\,(+B) - \theta\,(-B)$ for the p-wave, respectively.

a micro-channel plate (MCP) (Hamamatsu Photonics Corporation, MCP F4655) as a detector. The intensity of the reflected light from the multilayer mirror is measured by the detector as a function of rotation angle χ. It is expressed as

$$I\left(\chi\right)=\frac{r_p^2}{2}\left[2V\left(\alpha^2-1\right)\cos 2\varepsilon_{\mathrm{K}}\cos^2\left(\theta-\chi\right)+\alpha^2+1-V\left(\alpha^2-1\right)\cos 2\varepsilon_{\mathrm{K}}\right], \quad (3.37)$$

where α is the ratio, r_s/r_p, of reflectance amplitudes for the s- and p-waves [66, 67], and θ represents the azimuthal angle of the major axis of the elliptically polarization. When the light can be defined consistently by the Stokes parameters, the value of V is unity [66]. It is known as Malus's law that the intensity depends on the cosine square function on χ [66, 67]. In this study, χ was swept clockwise with the observer facing the beam. Using parameters $C_1\left(\varepsilon_{\mathrm{K}}\right)$ and $C_2\left(\varepsilon_{\mathrm{K}}\right)$, $I\left(\chi\right)$ is also rewritten simply as

$$I\left(\chi\right)=C_1\left(\varepsilon_{\mathrm{K}}\right)\cos 2\left(\chi-\theta\right)+C_2\left(\varepsilon_{\mathrm{K}}\right). \quad (3.38)$$

Since the polarization plane rotates inversely under opposite magnetic fields in the MOKE measurement, θ_{K} for the s-polarized incident light can be determined from the difference in the ellipsometry curves taken under opposite magnetic fields: $2\theta_{\mathrm{K}}^s=\theta\left(-B\right)-\theta\left(+B\right)$ in this geometry, as shown in Fig. 3.12(b). On the other hand, for the p-polarized incident light, it should be taken into account that r_{sp} includes $n_{-}-n_{+}$ whose sign is inverse to $n_{+}-n_{-}$ in r_{ps}, as shown in Eqs. (2.19) and (2.20). θ_{K}^p is calculated by $2\theta_{\mathrm{K}}^p=\theta\left(+B\right)-\theta\left(-B\right)$ based on the Onsager relations.

Chapter 4

Interface electronic structure at the topological insulator-ferrimagnetic insulator junction

In this chapter, we studied a magnetic interface between a three dimensional (3D) topological insulator (TI) and a magnetic material. This system is one of the interesting buried magnetic layers.

4.1 Introduction

As mentioned in Chapter 2, TIs are notable materials currently attracting a wide interest in both fundamental and applied research [68–70]. Although TIs show bulk insulating performance, they exhibit Dirac-like gapless bands at their surfaces [54–56, 71–74]. The surface state is ensured by time-reversal symmetry (TRS) and the spin polarization of the surface state electrons is locked to its momentum. Because these properties are resistant to non-magnetic external perturbations, TIs are expected to be promising materials for new spintronic devices [68–70].

By breaking TRS, TIs exhibit a number of interesting features, such as the gap-opening at the Dirac point [8, 75], the half-integer quantum Hall effect [76], the quantum anomalous Hall effect [77, 78], the topological magnetoelectric effect [76, 79], and the image magnetic monopole effect [80]. There are two methods for breaking the TRS; one is by doping magnetic impurities (Cr, Fe, and Mn) [75, 77, 78, 81, 82], and the other is by connecting TIs to magnetic materials such as Fe, Co, and EuS [8–12]. However, with the objective of device applications, magnetic metals in contact with TIs are not appropriate because the TI surface state is short circuited by the metallic materials [14].

Recently, it was suggested that a ferrimagnetic insulator, yttrium iron garnet (YIG, $Y_3Fe_5O_{12}$) with a Curie temperature (T_C) $\sim$ 550 K, has the potential to be an underlayer for magnetic TI films [13–16]. It was reported, from magneto-transport and magneto-optical measurements, that the temperature where the Bi_2Se_3 has a magnetic order (T_{MO}) reaches $\sim$ 130 K due to the proximity effect [13]. Furthermore, T_C of Cr-doped Bi_2Se_3 on YIG was found to be higher than that on a nonmagnetic substrate through magneto-transport and X-ray magnetic circular dichroism (XMCD) measurements [14, 15]. Understanding the mechanism of the proximity effect between TI and YIG is required to realize T_{MO} above room temperature (RT) for practical applications.

In this chapter, we present results of angle-resolved photoelectron spectroscopy (ARPES) and XMCD measurements for Bi_2Se_3 films on YIG. We have successfully observed the TI surface state in this Bi_2Se_3/YIG system and obtained direct evidence that the $3d$ electrons of Fe in YIG induce the proximity effect at the interface between TI and YIG.

4.2 Experiment

YIG(111) thin films (8.4 nm thick) were grown by pulsed laser deposition (PLD) on gadolinium gallium garnet (GGG) (111) substrates. Stoichiometric one-inch diameter YIG targets were prepared by mixing Y_2O_3 and Fe_2O_3, followed by ball milling, calcination, and sintering at 1400°C [83, 84]. The surfaces of the GGG substrates (Supplier: MTI Crystals, Inc.) were cleaned by ultrasonicating in acetone and then in isopropanol. PLD of YIG was carried out using a KrF coherent excimer laser ($\lambda = 248$ nm, 400 mJ pulses at 10 Hz pulse rate) at a growth rate of 3 nm/min (target-substrate distance: 85 mm) under 20 mTorr oxygen pressure (5×10^{-6} Torr base pressure), while 10 mm $\times$10 mm GGG(111) substrates were held at 650°C. After deposition and before cooling, the oxygen pressure in the chamber was increased to 500 Torr and then the films were annealed at 650°C. This annealing step improved the quality of the YIG films, as reported elsewhere [85]. The sample temperature was decreased to 200°C at 5°C/min in oxygen ambient, followed by natural cooling to RT.

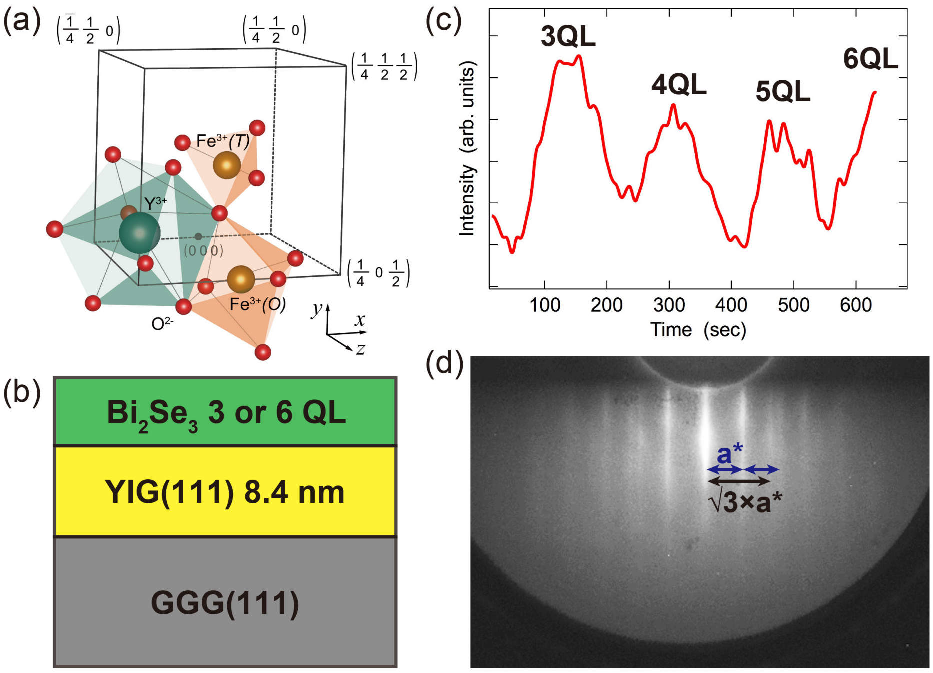

FIGURE 4.1: (a) A schematic drawing of the crystal structure of YIG. There are two sites for Fe ions, octahedral (O) and tetrahedral (T) sites. (b) A schematic drawing of the Bi_2Se_3 film prepared on a YIG(111)/GGG(111) sample. (c) The (00)-spot RHEED intensity oscillation during Bi_2Se_3 growth on the YIG film, taken at an electron energy of 15 keV. (d) The RHEED pattern of a 6 QL Bi_2Se_3/YIG sample. The symbol a* represents the reciprocal lattice constant of Bi_2Se_3.

Figure 4.1(a) shows the crystal structure of YIG (space group Ia_3d). The YIG formula unit can be written as follows: $\{Y_3^{3+}\}[Fe_2^{3+}](Fe_3^{3+})O_{12}^{2-}$. The nonmagnetic yttrium ions (Y^{3+}) occupy 24c sites. Fe^{3+} ions occupy 16a (octahedral, O) and 24d (tetrahedral, T) lattice sites in the ratio of 2 : 3, respectively. The spins of these sites are antiparallel and as a result, the unit cell is ferrimagnetic [86].

Figure 4.1(b) shows a schematic drawing of a Bi_2Se_3/YIG heterojunction. Bi_2Se_3 films were grown on a YIG film prepared on GGG (YIG/GGG) using Bi and Se effusion cells. At first, 2 quintuple layers (QLs) of Bi_2Se_3 were grown on YIG at 150°C and subsequently annealed at 300°C. Then further Bi and Se depositions were made at a sample temperature of 250°C. The thickness of the Bi_2Se_3 films was controlled from 3 to 6 QL by observing reflection high-energy electron diffraction (RHEED) intensity oscillations, as shown in Fig. 4.1(c). After the deposition, the samples were annealed at 250°C for 15 min to improve the crystalline quality. Figure 4.1(d) presents the RHEED pattern of the 6 QL Bi_2Se_3/YIG/GGG sample. Referred to the (00)-rod, streaks are identified at 2a* and $\sqrt{3}\times$a* where a* represents the reciprocal lattice constant of

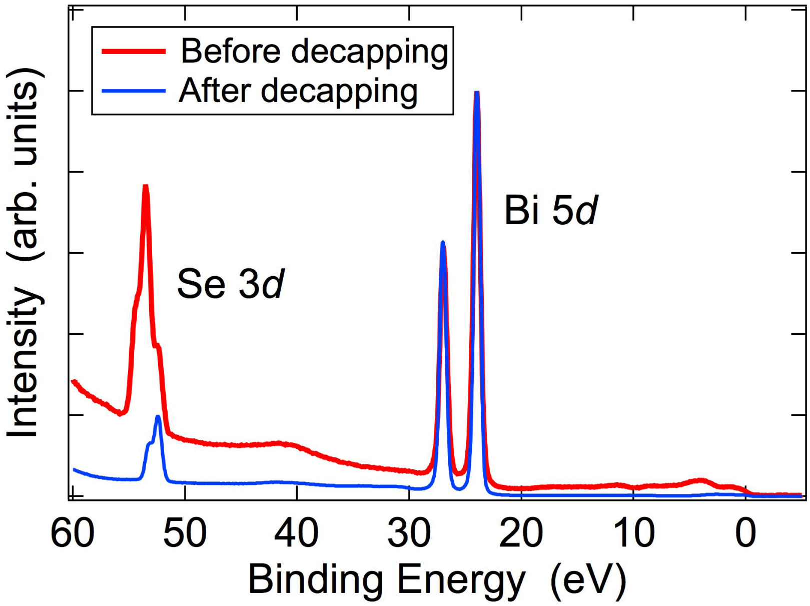

FIGURE 4.2: Core level photoelectron spectroscopy spectra, taken at $h\nu =$ 87.6 eV, of a 6 QL Bi_2Se_3/YIG sample before (red) and after (blue) decapping. These spectra were normalized to the Bi $5d_{5/2}$ peak.

Bi_2Se_3. The pattern indicates that the Bi_2Se_3 films have a multi-domain structure such as a ⟨111⟩-textured structure [87]. Finally, the sample surface was capped with a 30 nm-thick Se layer in order to transfer the sample wafer in air to the ARPES chamber. Removal of the capping layer was accomplished by annealing at 190°C for $\sim$ 10 min in an ultra high vacuum (UHV) chamber prior to ARPES experiment.

The ARPES experiment was performed at the VUV-Photoemission beamline at Elettra, Italy. Figure 4.2 shows the core level photoelectron spectra of the 6 QL Bi_2Se_3/YIG sample before and after the decapping procedure. In contrast to a large and broad peak structure of the Se 3*d* peak for the capped sample, a clean Bi_2Se_3 surface shows only a single Se 3*d* doublet component that is split by the spin-orbit (SO) interaction, as reported previously [88]. On the other hand, no apparent change was observed for the spectral features of the Bi 5*d* core level. These observations indicate that the present capping/decapping procedure was appropriate and a clean Bi_2Se_3 film is left after the decapping.

XMCD measurements of the Bi_2Se_3/YIG samples were made at the Fe *L*-edge at RT and 20 K. The experiment was made at the high-brilliance soft X-ray beamline [60], BL07LSU, at SPring-8, Japan. A magnetic field of 0.24 T was applied by a retractable permanent magnet. The XMCD was measured at the Fe $L_{2,3}$-shell absorption edge of

YIG by the total electron yield (TEY) and total fluorescence yield (TFY) modes. In the TFY mode, fluorescence from the sample was detected by a silicon drift detector (SDD), as shown in Fig. 3.10. XMCD spectra were derived from the difference between the two absorption spectra obtained by circular polarized light of opposite helicities, where the beam direction was set parallel to the magnetic field orientation and to the surface normal direction.

4.3 Results and discussion

4.3.1 Angle-resolved photoelectron spectroscopy (ARPES) study

Figure 4.3(a) shows the momentum ($k_{//}$: parallel to the sample surface) distribution curves (MDCs) of the ARPES spectra around the $\bar{\Gamma}$ point, taken at $h\nu = 52.4$ eV, at RT. In the ARPES experiment, linear polarized light was incident onto the sample in the *p*-configuration. In the figure, it can be seen that the two peaks in the MDCs at the Fermi energy ($E_{\rm F}$) approach with increasing binding energy ($E_{\rm B}$) and overlap each other at $E_{\rm B} = 0.38$ eV, followed by separation at higher $E_{\rm B}$. These results unambiguously indicate band-crossing. The MDCs at RT in Fig. 4.3(a) and $T = 30$ K (not shown) were fitted by two Gaussian peaks and the peak positions are plotted in the photoelectron band diagrams in Figs. 4.3(b) and (c). At $T = 30$ K and RT, the surface state band shows the Dirac cone dispersion around the $\bar{\Gamma}$ point with the Dirac point at $E_{\rm B} = 0.38$ eV. The band-dispersion curves were assigned to those of the Dirac surface state bands of the Bi_2Se_3 film as reported previously [55, 74]. The Fermi velocity of this system is $v_{\rm F} = 5.1 \times 10^5$ m/s and this value agrees with previous studies [54, 71, 72].

For comparison, the photoelectron band diagram, taken at $h\nu = 23.1$ eV, is also shown in Fig. 4.3(d). The observed band between $E_{\rm F}$ and 0.2 eV is assigned to the bulk conduction band of Bi_2Se_3, as reported previously [55, 74] and it crosses the $E_{\rm F}$, indicating the *n*-type doped nature. The electronic structures of the surface and bulk states are essentially similar to the previous ARPES results of Bi_2Se_3 films on different substrates [55, 56, 71–74]. Due to the TI nature of the Bi_2Se_3 film [69, 70, 80], the existence of the surface state at the film/vacuum interface suggests its presence also at the junction (interface) with the insulator YIG film. Moreover, Fig. 4.3(d) implies that the Bi_2Se_3 bulk conduction band crosses $E_{\rm F}$ at the Bi_2Se_3/YIG interface. It is notable that the surface state band structure does not change with the temperature across $T_{\rm MO} \sim 130$ K [13], as shown in Fig. 4.3.

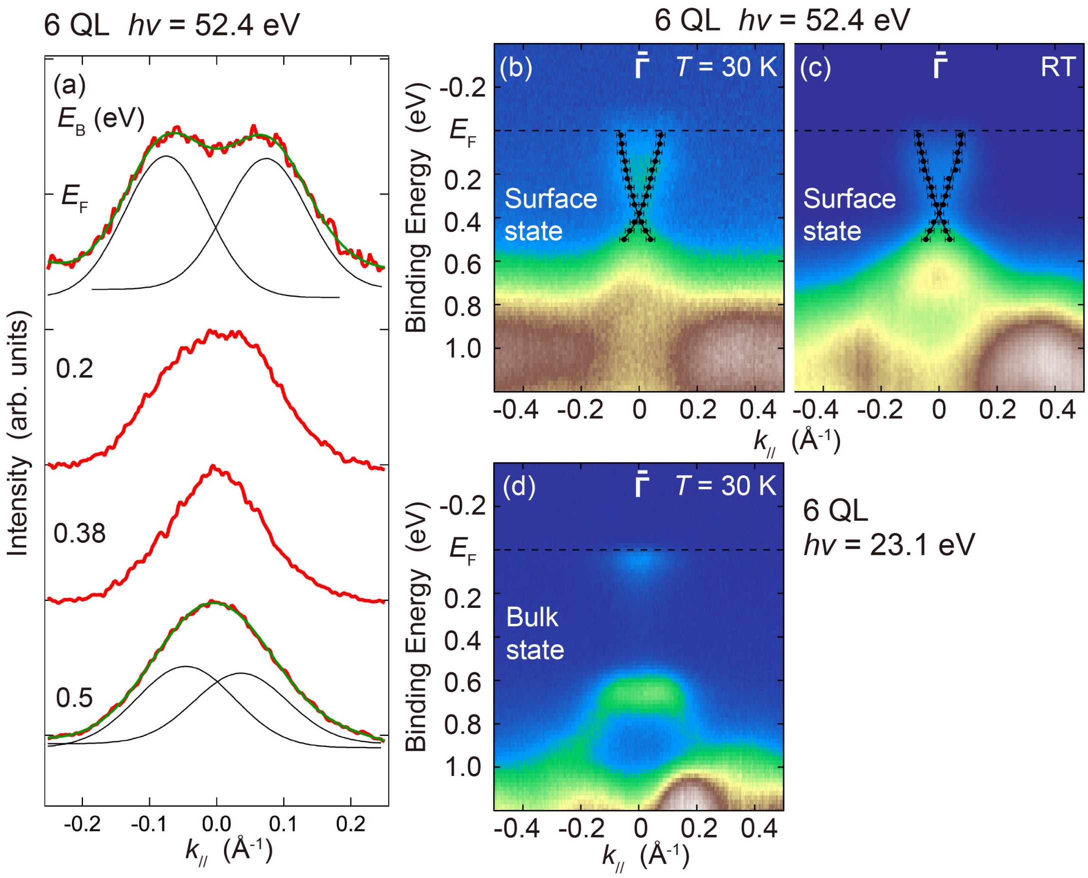

FIGURE 4.3: (a) Photoelectron momentum distribution curves (MDCs), taken at $h\nu = 52.4$ eV, for the 6 QL Bi_2Se_3/YIG sample at RT (red solid lines). The solid black and green lines indicate the two-peak fitting curves. (b, c) Photoelectron band diagrams around $\bar{\Gamma}$ for the 6 QL Bi_2Se_3/YIG sample at (b) $T = 30$ K and (c) RT ($h\nu = 52.4$ eV). The solid circles correspond to the peak position from the MDCs and the black lines are fits. (d) ARPES spectra of the 6 QL Bi_2Se_3/YIG sample at $T = 30$ K ($h\nu = 23.1$ eV).

4.3.2 X-ray magnetic circular dichroism (XMCD) study

Figures 4.4(a) and (b) show the Fe $2p$ X-ray absorption spectra (a) and XMCD spectra (b) by the TEY mode. The spectral shapes are mostly in agreement with those of the Cr-doped Bi_2Se_3/YIG sample reported by Liu *et al.* [14, 15]. Since the probing depth of the present XMCD measurements using the TEY mode is about 5 $\sim$ 10 nm, as described in Chapter 3, not much different from the thickness of 3 nm (3 QL) and 6 nm (6 QL) Bi_2Se_3 [17, 89], the XMCD signals are thought to be essentially resulting from the Fe atoms near the Bi_2Se_3/YIG boundary. The positive XMCD peaks at $h\nu = 708$ and 710 eV and the negative peak at $h\nu = 709.5$ eV suggest opposite spin directions for the Fe atoms at two different sites in the YIG crystal, O (2 per formula unit) and T

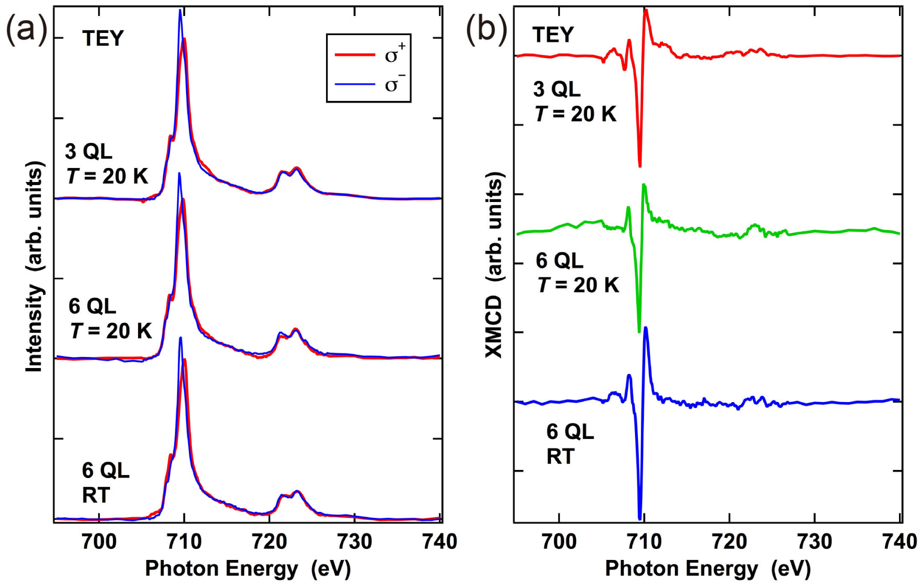

FIGURE 4.4: (a) XAS spectra of the 3 and 6 QL Bi_2Se_3/YIG samples obtained by the TEY mode at RT and 20 K. The solid red and blue lines represent the spectra taken with circular polarized light of plus and minus helicity (σ^+, σ^-), respectively. (b) XMCD spectra of 3 QL Bi_2Se_3/YIG at $T = 20$ K (red), 6 QL Bi_2Se_3/YIG at $T = 20$ K (green), and 6 QL Bi_2Se_3/YIG at RT (blue) obtained by the TEY mode.

sites (3 per formula unit), as expected for the ferrimagnet. In the present measurement configuration, the macroscopic magnetic direction of the ferrimagnetic YIG film shows a negative peak for the Fe (T) site [14, 15]. Furthermore, we notice a slight structure at the L_3 pre-edge as described below.

The upper curves of Fig. 4.5(a) are the enlarged XAS spectra of the 6 QL Bi_2Se_3/YIG at RT obtained by the TEY mode at $h\nu = 705 \sim 708$ eV. One can notice a spectral feature at $h\nu \sim 706.5$ eV in the σ^+ spectrum. Compared with the previous X-ray absorption study [90], the spectral feature is likely assigned to the $Fe^{\delta+}$ ($\delta < 3$) state in the YIG crystal. On the other hand, the spectra in Fig. 4.5(b) and the lower curves in Fig. 4.5(a) are the XAS results obtained by the TFY mode and they essentially have very similar spectral feature as those taken by the TEY mode, except for the pre-edge structure at $h\nu = 706.5$ eV. Since the probing depth in the TFY mode is $10 \sim 100$ nm, as described in Chapter 3 [17], the spectra obtained by this mode mainly give information from Fe in the internal bulk region of YIG. These results indicate the possible existence of the $Fe^{\delta+}$ state at the Bi_2Se_3/YIG interface. It was reported that $Fe^{\delta+}$ states were produced by oxygen deficiency at the surface or interface of YIG [91, 92].

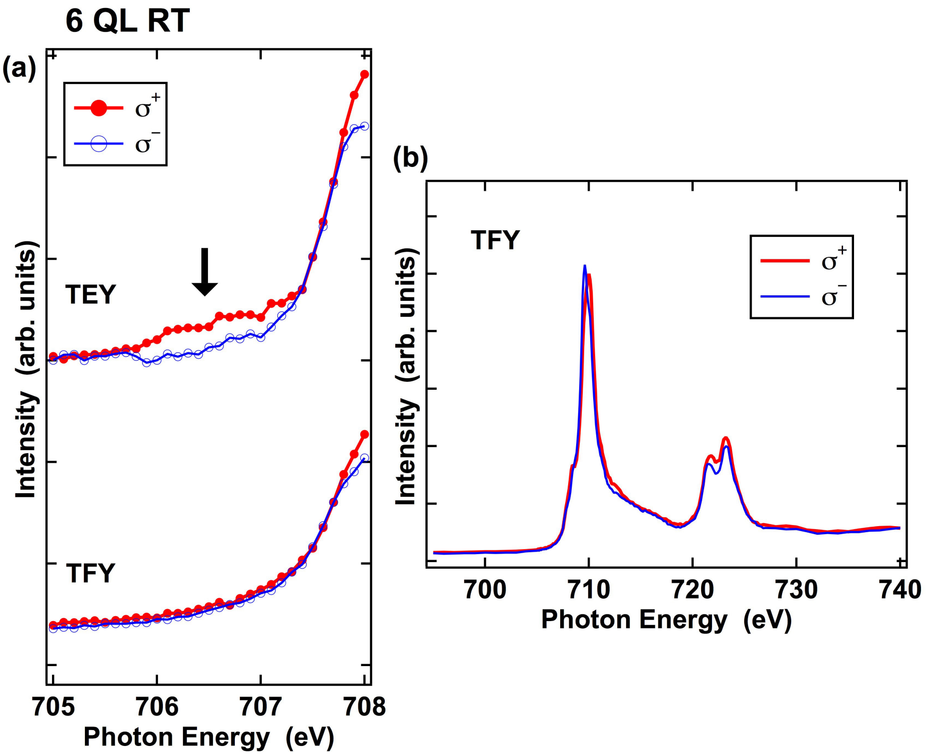

FIGURE 4.5: (a) Enlarged XAS spectra of 6 QL Bi_2Se_3/YIG at RT in the absorption edge region obtained by the TEY mode (upper) and the TFY mode (bottom). Intensity enhancement is observed at the pre-edge in the σ^+ TEY spectrum (indicated by arrow). The red and blue lines represent the spectra taken with σ^+ and σ^-, respectively. (b) XAS spectra of 6 QL Bi_2Se_3/YIG at RT obtained by the TFY mode.

4.3.3 Interaction model at the interface

From the experimental results shown above, magnetic order of Bi_2Se_3 at the interface is most probably associated with the interface spin polarized states of the Bi_2Se_3 film and localized spin states of the interface Fe^{3+} in the YIG film. Thus, the proximity effect would be modeled as their interactions at the boundary. Such interface interaction has been already investigated theoretically for a similar system that is composed of a Bi_2Se_3 film and an EuS substrate [93]. When the TI film has a Dirac surface state with a gap at the Dirac point by breaking the TRS, these delocalized spins were found to experience an exchange interaction with the localized spins of the $4f$ electrons in the Eu^{2+} ions [93]. Moreover, it was found that bulk (p_z-orbital) states of the Bi_2Se_3 film also contribute to the spin-coupling between the TI and the magnetic material when E_F is located above the minimum of the bulk conduction band [93]. By analogy, the magnetic order of Bi_2Se_3 at the interface can be understood as an exchange interaction

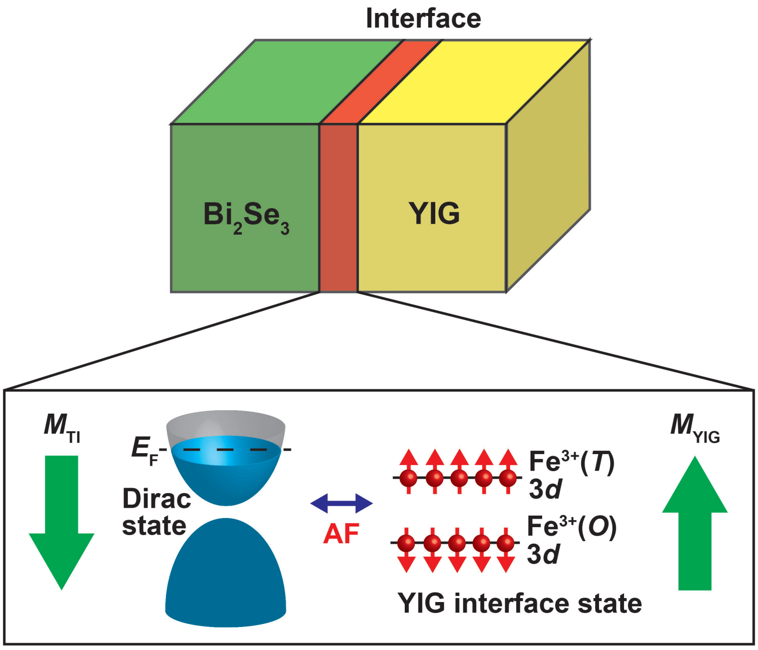

FIGURE 4.6: A schematic drawing of the proximity effect at the Bi_2Se_3 and YIG interface. The origin is the antiferromagnetic (AF) exchange interaction between the spin polarized electrons of the Bi_2Se_3 film and the localized $3d$ electrons of the Fe^{3+} sites. The Bi_2Se_3 Dirac surface state band produces gap-opening at the Dirac point. The macroscopic magnetic moments of Bi_2Se_3 ($\boldsymbol{M}_{\mathrm{TI}}$) and YIG ($\boldsymbol{M}_{\mathrm{YIG}}$) have opposite orientations from each other.

between the spin polarized electrons in the (gapped) Dirac surface state of the Bi_2Se_3 film and the localized $3d$ electrons of Fe^{3+} in the YIG film [11, 13], as shown in Fig. 4.6. Moreover, there is also a contribution from the bulk electrons in the Bi_2Se_3 film since the bulk conduction band crosses E_{F} [Fig. 4.3(d)].

Judging from the sign of the XMCD signal, one can naturally assume that the $Fe^{\delta+}$ state originates from the Fe atom at the O site. At a surface, the Fe ions are likely reduced by oxygen vacancies [91, 92] that are probably formed during the film growth process. The $Fe^{\delta+}$ ions seem to occupy a few percent of the Fe sites, as estimated from the XAS intensity ratio. The $3d$ electrons at the Fe (O) and Fe (T) sites in YIG have opposite spin orientations from each other and they individually have antiferromagnetic interactions with the Dirac electrons of Bi_2Se_3 because all Fe $3d$ electron states are occupied by the electrons with parallel spin due to the Hund's rules. This results in macroscopic configuration of the opposite magnetic moments between the Bi_2Se_3 film and the YIG substrate [13], as schematically shown in Fig. 4.6. Since the spin magnetic moment at the Fe^{3+} (O) site is opposite to that of YIG and the magnetic moment of $Fe^{\delta+}$ is smaller than that of Fe^{3+}, one expects that the change to $Fe^{\delta+}$ at the O site enhances the magnetic order at the Bi_2Se_3/YIG interface. On the other hand, the Fe ions could also be reduced at the T site. However, it is not possible to argue the formation of the $Fe^{\delta+}$ state at the T site since the corresponding faint signal of this impurity in the XAS spectra [Figs. 4.4(a) and 4.5(a)] will be completely overlapping and covered with the large spectral peak of the Fe^{3+} (O) state at $h\nu \sim 708$ eV. Because decrease of the spin magnetic moment at the Fe (T) site results in suppression of the interface magnetic order, one should conclude that it is unnecessary to increase the number of the $Fe^{\delta+}$ state at the interface. Nevertheless, our result implies a possible improvement of the interface magnetic order by the selective reduction of the Fe^{3+} state at the Fe (O) site.

It is notable that not only investigating the details of the $Fe^{\delta+}$ state but also an appropriate analysis to determine atomic structure at the Bi_2Se_3/YIG heterojunction is needed in order to conduct a first-principles calculation to properly understand the scenario.

4.4 Conclusion

In summary, we provide evidence of the surface state of the Bi_2Se_3 film on YIG by ARPES and the significance of the Fe^{3+} state for magnetic order of the Bi_2Se_3 at the interface by Fe $L_{2,3}$-edge XMCD. The origin of the proximity effect is likely described in terms of the exchange interaction between the localized Fe^{3+} $3d$ electrons in the YIG film and the delocalized electrons of the Dirac surface state and the bulk state in the Bi_2Se_3 film. In addition, we succeeded in showing the possibility that controlling the valence number of the Fe ions at the interface may be able to change the interface magnetic property. This study plays a part in understanding the proximity effect between TI and YIG, contributing to the realization of TI-based devices.

However, this study only shows the indirect results of the magnetic TI at the interface. To unveil the mechanism of magnetic order in TI perfectly, a direct measurement by bulk sensitive methods with high accuracy is required.

Chapter 5

Contents in this chapter will be published in five years and are not opened to the public now.
本章については、5年以内に雑誌等で刊行予定のため、現在非公開。

Chapter 6

Contents in this chapter will be published in five years and are not opened to the public now.
本章については、5年以内に雑誌等で刊行予定のため、現在非公開。

Chapter 7

Contents in this chapter will be published in five years and are not opened to the public now.
本章については、5年以内に雑誌等で刊行予定のため、現在非公開。

Chapter 8

Summary and future prospect

8.1 Summary

In the present thesis, the magnetism of buried layers was investigated and their attracting properties were observed. In order to get abundant information on them, which is difficult to obtain by the existing methods, we developed the new light source and methods in the soft X-ray energy region with the polarization modulation. We demonstrate the performance of this method and show the new information of magnetism using the polarization modulation.

In Chapter 4, the interface electron state at the junction between a three dimensional (3D) topological insulator (TI) film, Bi_2Se_3, and a ferrimagnetic insulator film, $Y_3Fe_5O_{12}$ (YIG), was investigated by measurements of angle-resolved photoelectron spectroscopy (ARPES) and X-ray magnetic circular dichroism (XMCD). The magnetic TI should appear at the interface derived from the proximity effect, which is expected to be promising materials for new spintronic devices. The surface state of the Bi_2Se_3 film was directly observed by ARPES and it has a Dirac-like band structure like as those of other Bi_2Se_3 grown on different substrates. By XMCD measurements, the localized $3d$ spin states of Fe^{3+} in the YIG film were confirmed. Furthermore, it should be also reported that the valence number of the Fe ions in the YIG film varies and it could affect the magnetism at the interface. From these results, we propose the interface model that the proximity effect is likely described in terms of the exchange interaction between the localized Fe $3d$ electrons in the YIG film and the delocalized electrons of the surface and bulk states in the Bi_2Se_3 film observed by ARPES. This study shows the importance of the magnetism at the interface that it is ordinarily difficult to observe in detail by the common techniques.

In Chapter 5, the L-edge resonant magneto-optical Kerr effect (MOKE) of a buried Fe film was investigated by the rotating-analyzer ellipsometry (RAE) and the Kerr rotation angle (θ_K) obtained by the experiment was compared with those obtained from two theoretical simulations. The resonant MOKE measurement in the soft X-ray energy region is a powerful method to detect the magnetism at buried layers because of using a reflected light and the resonant enhancement. In contrast to MOKE with visible light, resonant MOKE also has element-selectivity. The sign reversal of θ_K between the L_3- and L_2-edges was first observed in the experiment. Furthermore, it was consistent with the classical electromagnetic simulation using the empirical optical constants. On the other hand, the θ_K spectrum at the L_3-edge, including the fine features, was reproduced by the quantum theoretical calculation of the Fe $2p$–$3d$ resonant elastic scattering. However, a large peak between the L_3- and L_2-edges, which was also obtained from the quantum calculation, is not found in the experimental spectrum. These features likely originate from the quantum interference effect during the resonant scattering process that is described by the Kramers-Heisenberg formula. The large peak could be reduced by the decoherence process of the other optical transitions and the inelastic scattering process in the actual sample. In addition, to the best of our knowledge, the polarization dependence of θ_K was also reported for the first time in the soft X-ray energy region. We succeeded in showing the usefulness of resonant MOKE, its quantum mechanism that shapes the θ_K spectrum, and the tasks to improve quantum calculations.

In Chapter 6 and 7, we present the main subject of this thesis. We developed the new polarization modulated soft X-ray at SPring-8 BL07LSU fully utilizing the performance of the segmented cross undulator, especially, the phase shifter composed of a permanent magnet and an electromagnet. Its performance was confirmed by the XMCD measurements with the modulated light for the FePt film and the $(\mathrm{Bi}_{1-x}\mathrm{Sb}_x)_2\,\mathrm{Te}_3$/YIG samples. XMCD was obtained by extracting the p component, which is the same frequency as the polarization modulation, from the sample current signal and its high sensitivity and accuracy were shown. Moreover, we designed the new method combining the resonant MOKE measurement and the polarization modulated light in the soft X-ray region. Adding the merits of the resonant MOKE measurement, this method enables us to measure θ_K and the ellipticity (ε_K) simultaneously and high accuracy due to extracting the p and $2p$ components from the detected signal. Furthermore, since θ_K and ε_K are derived from the optical rotation and the magnetic circular dichroism

(MCD), respectively, the off-diagonal components of the permittivity, which have magnetic information of materials, can be determined completely including both of the real and imaginary parts. In fact, we succeeded in first measuring the θ_K and ε_K spectra of the Fe film simultaneously and they are consistent with the fact that the spectra of θ_K and ε_K are connected by the Kramers-Kronig relations. Although we have depended on the simulation to obtain the value of permittivity in the soft X-ray energy region in the past, the experimental complex permittivity can be determined completely by our developed resonant MOKE method in this study. It is clear that the present study opened the new field of magnetism research.

8.2 Future prospect

In the discussion above, the new methods were developed by combining the magneto-optical effect with the polarization modulated soft X-ray. The XMCD measurement with the polarization modulation, which enables us to observe a weak MCD, can be applied to TI/magnetic material systems. In this thesis, the MCD of Fe^{3+} in YIG was observed and we considered its effect on the magnetism of TI. To get a proper understanding of the proximity effect, it is required to observe the magnetism of TI directly. Comparing with the previous study reported by M. Ye *et al.* [118], the MCD of magnetic TI appearing only at the interface with a magnetic material should be much weaker than that of a magnetic element doped TI, such as Cr-doped $(\mathrm{Bi}_{1-x}\mathrm{Sb}_x)_2\,\mathrm{Te}_3$. However, the XMCD measurement with the modulated light should become a method that can detect the weak signal from the interface by an optimization of the undulator at SPring-8 BL07LSU. $(\mathrm{Bi}_{1-x}\mathrm{Sb}_x)_2\,\mathrm{Te}_3$ on YIG that studied in Chapter 6 would be investigated by the method and the MCD of Sb or Te in the TI should be observed directly like as the previous study [118]. It leads to figure out the mechanism of the proximity effect completely.

In addition, the MOKE measurement with the polarization modulation enables us to measure the complex permittivity with element-selectivity in the soft X-ray energy region, as discussed in Chapter 7. The permittivity of any kind of magnetic material can be measured by this method with optimizations of the segmented cross undulator and the multilayer mirror without the sample limitation like as the transmission and diffraction methods. Permittivity would be useful to understand the electronic structures and the optical transitions of the magnetic materials both of experimentally and theoretically. Moreover, using the permittivity obtained experimentally can also develop optical designs that have relied on the simulations in the soft X-ray region until now. It is also expected that the determination of permittivity would be used for the material design, and the light induced spin-flip by the inverse Faraday effect [129, 130] could be investigated, thus, this method can be applied to a time evolution study with high harmonic generation (HHG) laser and X-ray free electron laser (XFEL) in the future.

Publications

Publications included in this thesis

1. **Generation of polarization modulated soft X-ray waves and determination of element-specific complex permittivity**
   Y. Kubota, Y. Hirata, J. Miyawaki, S. Yamamoto, R. Hobara, Sh. Yamamoto, K. Yamamoto, T. Someya, K. Takubo, Y. Yokoyama, M. Araki, M. Taguchi, Y. Harada, H. Wadati, M. Tsunoda, R. Kinjo, A. Kagamihata, T. Seike, M. Takeuchi, T. Tanaka, S. Shin, and I. Matsuda
   to be submitted for publication.

2. **Study of L-edge resonant magneto-optical Kerr effect of a buried Fe nanofilm**
   Y. Kubota, M. Taguchi, Sh. Yamamoto, T. Someya, Y. Hirata, K. Takubo, M. Araki, M. Fujisawa, K. Yamamoto, Y. Yokoyama, S. Yamamoto, M. Tsunoda, H. Wadati, S. Shin, and I. Matsuda
   submitted to Physical Review B.

3. **Polarization dependence of resonant magneto-optical Kerr effect measured by two types of figure-8 undulators**
   Y. Kubota, Sh. Yamamoto, T. Someya, Y. Hirata, K. Takubo, M. Araki, M. Fujisawa, K. Yamamoto, Y. Yokoyama, M. Taguchi, S. Yamamoto, M. Tsunoda, H. Wadati, S. Shin, and I. Matsuda
   Journal of Electron Spectroscopy and Related Phenomena, in press.
   DOI: 10.1016/j.elspec.2016.11.008

4. **Interface electronic structure at the topological insulator-ferrimagnetic insulator junction**
   Y. Kubota, K. Murata, J. Miyawaki, K. Ozawa, M. C. Onbasli, T. Shirasawa, B. Feng, S. Yamamoto, R.-Y. Liu, S. Yamamoto, S. K. Mahatha, P. Sheverdyaeva,

P. Moras, C. A. Ross, S. Suga, Y. Harada, K. L. Wang, and I. Matsuda
Journal of Physics: Condensed Matter **29**, 55002 (2017).

Bibliography

[1] M. Faraday, Philosophical Transactions of the Royal Society of London **136**, 1 (1846).

[2] J. Kerr, Report of the British Association for the Advancement of Science p. 40 (1876).

[3] J. Kerr, Philosophical Magazine Series 5 **3**, 321 (1877).

[4] P. M. Oppeneer, in *Handbook of Magnetic Materials*, edited by K. H. J. Buschow (Elsevier, Amsterdam, 2001), Vol. 13.

[5] B. Thole, P. Carra, F. Sette, and G. van der Laan, Physical Review Letters **68**, 1943 (1992).

[6] P. Carra, B. Thole, M. Altarelli, and X. Wang, Physical Review Letters **70**, 694 (1993).

[7] C. T. Chen, Y. U. Idzerda, H. J. Lin, N. V. Smith, G. Meigs, E. Chaban, G. H. Ho, E. Pellegrin, and F. Sette, Physical Review Letters **75**, 152 (1995).

[8] L. A. Wray, S.-Y. Xu, Y. Xia, D. Hsieh, A. V. Fedorov, Y. S. Hor, R. J. Cava, A. Bansil, H. Lin, and M. Z. Hasan, Nature Physics **7**, 32 (2010).

[9] J. Li, Z. Y. Wang, A. Tan, P.-A. Glans, E. Arenholz, C. Hwang, J. Shi, and Z. Q. Qiu, Physical Review B **86**, 054430 (2012).

[10] D. West, Y. Y. Sun, S. B. Zhang, T. Zhang, X. Ma, P. Cheng, Y. Y. Zhang, X. Chen, J. F. Jia, and Q. K. Xue, Physical Review B **85**, 081305 (2012).

[11] P. Wei, F. Katmis, B. A. Assaf, H. Steinberg, P. Jarillo-Herrero, D. Heiman, and J. S. Moodera, Physical Review Letters **110**, 186807 (2013).

[12] Q. I. Yang, M. Dolev, L. Zhang, J. Zhao, A. D. Fried, E. Schemm, M. Liu, A. Palevski, A. F. Marshall, S. H. Risbud, et al., Physical Review B **88**, 081407 (2013).

[13] M. Lang, M. Montazeri, M. C. Onbasli, X. Kou, Y. Fan, P. Upadhyaya, K. Yao, F. Liu, Y. Jiang, W. Jiang, et al., Nano Letters **14**, 3459 (2014).

[14] W. Liu, L. He, Y. Xu, K. Murata, M. C. Onbasli, M. Lang, N. J. Maltby, S. Li, X. Wang, C. A. Ross, et al., Nano Letters **15**, 764 (2014).

[15] W. Liu, L. He, Y. Zhou, K. Murata, M. C. Onbasli, C. A. Ross, Y. Jiang, Y. Wang, Y. Xu, R. Zhang, et al., AIP Advances **6**, 055813 (2016).

[16] Z. Jiang, F. Katmis, C. Tang, P. Wei, J. S. Moodera, and J. Shi, Applied Physics Letters **104**, 222409 (2014).

[17] J. Stöhr, *NEXAFS Spectroscopy* (Springer-Verlag, Berlin, 1992), p. 122.

[18] H.-C. Mertins, D. Abramsohn, A. Gaupp, F. Schäfers, W. Gudat, O. Zaharko, H. Grimmer, and P. M. Oppeneer, Physical Review B **66**, 184404 (2002).

[19] C. Kao, J. Hastings, E. Johnson, D. Siddons, G. Smith, and G. Prinz, Physical Review Letters **65**, 373 (1990).

[20] H.-C. Mertins, F. Schäfers, X. Le Cann, A. Gaupp, and W. Gudat, Physical Review B **61**, R874 (2000).

[21] J. Kuneš, P. M. Oppeneer, H.-C. Mertins, F. Schäfers, A. Gaupp, W. Gudat, and P. Novák, Physical Review B **64**, 174417 (2001).

[22] J. Kortright, D. Awschalom, J. Stöhr, S. Bader, Y. Idzerda, S. Parkin, I. K. Schuller, and H.-C. Siegmann, Journal of Magnetism and Magnetic Materials **207**, 7 (1999).

[23] K.-S. Lee, S.-K. Kim, and J. B. Kortright, Applied Physics Letters **83**, 3764 (2003).

[24] H.-C. Mertins, S. Valencia, D. Abramsohn, A. Gaupp, W. Gudat, and P. M. Oppeneer, Physical Review B **69**, 064407 (2004).

[25] S. Valencia, H.-C. Mertins, D. Abramsohn, A. Gaupp, W. Gudat, and P. M. Oppeneer, Physica B: Condensed Matter **345**, 189 (2004).

[26] S.-K. Kim, K.-S. Lee, J. B. Kortright, and S.-C. Shin, Applied Physics Letters **86**, 102502 (2005).

[27] M. F. Tesch, M. C. Gilbert, H.-C. Mertins, D. E. Bürgler, U. Berges, and C. M. Schneider, Applied Optics **52**, 4294 (2013).

[28] Sh. Yamamoto, M. Taguchi, M. Fujisawa, R. Hobara, S. Yamamoto, K. Yaji, T. Nakamura, K. Fujikawa, R. Yukawa, T. Togashi, et al., Physical Review B **89**, 064423 (2014).

[29] Sh. Yamamoto, M. Taguchi, T. Someya, Y. Kubota, S. Ito, H. Wadati, M. Fujisawa, F. Capotondi, E. Pedersoli, M. Manfredda, et al., Review of Scientific Instruments **86**, 083901 (2015).

[30] H. Gotsis and P. Strange, Journal of Magnetism and Magnetic Materials **140-144**, 2171 (1995).

[31] J. B. Kortright and S.-K. Kim, Physical Review B **62**, 12216 (2000).

[32] T. Katayama, N. Nakajima, N. Okusawa, Y. Miyauchi, T. Koide, T. Shidara, Y. Suzuki, and S. Yuasa, Journal of Magnetism and Magnetic Materials **177-181**, 1251 (1998).

[33] K. Sato, Japanese Journal of Applied Physics **20**, 2403 (1981).

[34] K. Sato, H. Kida, and T. Kamimura, Journal of the Magnetics Society of Japan **11**, S1 113 (1987).

[35] W. Voigt, Annalen der Physik und Chemie **67**, 345 (1899).

[36] R. M. Bozorth, *Ferromagnetism* (D. Van Nostrand Co. Inc., New York, 1951), p. 441.

[37] J. W. D. Connolly, Physical Review **159**, 415 (1967).

[38] S. Wakoh and J. Yamashita, Journal of the Physical Society of Japan **21**, 1712 (1966).

[39] H. Burkhard and J. Jaumann, Zeitschrift für Physik A Hadrons and nuclei **235**, 1 (1970).

[40] X. X. Zhang, J. Schoenes, and P. Wachter, Solid State Communications **39**, 189 (1981).

[41] C. L. Kane and E. J. Mele, Physical Review Letters **95**, 146802 (2005).

[42] C. L. Kane and E. J. Mele, Physical Review Letters **95**, 226801 (2005).

[43] B. A. Bernevig and S.-C. Zhang, Physical Review Letters **96**, 106802 (2006).

[44] L. Fu, C. Kane, and E. Mele, Physical Review Letters **98**, 106803 (2007).

[45] J. Moore and L. Balents, Physical Review B **75**, 121306 (2007).

[46] R. Roy, Physical Review B **79**, 195322 (2009).

[47] L. Fu and C. L. Kane, Physical Review B **74**, 195312 (2006).

[48] L. Fu and C. L. Kane, Physical Review B **76**, 045302 (2007).

[49] C. Sabater, D. Gosálbez-Martínez, J. Fernández-Rossier, J. G. Rodrigo, C. Untiedt, and J. J. Palacios, Physical Review Letters **110**, 176802 (2013).

[50] M. Konig, S. Wiedmann, C. Brune, A. Roth, H. Buhmann, L. W. Molenkamp, X.-L. Qi, and S.-C. Zhang, Science **318**, 766 (2007).

[51] A. Roth, C. Brune, H. Buhmann, L. W. Molenkamp, J. Maciejko, X.-L. Qi, and S.-C. Zhang, Science **325**, 294 (2009).

[52] B. A. Bernevig, T. L. Hughes, and S.-C. Zhang, Science **314**, 1757 (2006).

[53] M. König, H. Buhmann, L. W. Molenkamp, T. Hughes, C. X. Liu, X. L. Qi, and S. C. Zhang, Journal of the Physical Society of Japan **77**, 031007 (2008).

[54] H. Zhang, C.-X. Liu, X.-L. Qi, X. Dai, Z. Fang, and S.-C. Zhang, Nature Physics **5**, 438 (2009).

[55] Y. Xia, D. Qian, D. Hsieh, L. Wray, A. Pal, H. Lin, A. Bansil, D. Grauer, Y. S. Hor, R. J. Cava, et al., Nature Physics **5**, 398 (2009).

[56] D. Hsieh, Y. Xia, D. Qian, L. Wray, J. H. Dil, F. Meier, J. Osterwalder, L. Patthey, J. G. Checkelsky, N. P. Ong, et al., Nature **460**, 1101 (2009).

[57] E. E. Koch, D. E. Eastman, and Y. Farge, *Handbook on Synchrotron Radiation*, edited by E. E. Koch (North-Holland Publishing Company, Amsterdam, 1983), Vol. 1A, p. 1-63; S. Krinsky, M. L. Perlman, and R. E. Watson, *ibid.*, p. 65-171.

[58] M. Terasawa and M. Kihara, *Applications of Synchrotron Radiation to Materials Analysis*, edited by H. Saisho and Y. Gohshi (Elsevier Science B. V., Amsterdam, 1996), p. 1-78.

[59] SPring-8 HP, URL `http://www.spring8.or.jp/en/about_us/whats_sp8/facilities/bl/light_source_optics/sources/`.

[60] S. Yamamoto, Y. Senba, T. Tanaka, H. Ohashi, T. Hirono, H. Kimura, M. Fujisawa, J. Miyawaki, A. Harasawa, T. Seike, et al., Journal of Synchrotron Radiation **21**, 352 (2014).

[61] S. Hüfner, *Photoelectron Spectroscopy* (Springer, 1995).

[62] A. Einstein, Annalen der Physik **322**, 132 (1905).

[63] A. Zangwill, *Physics at surfaces* (Cambridge University Press, 1988).

[64] J. Stöhr and H. C. Siegmann, *Magnetism: From Fundamentals to Nanoscale Dynamics* (Springer, Heidelberg, 2006), Solid-State Sciences, Vol. 152.

[65] S. W. Lovesey and S. P. Collins, in *X-ray Scattering and Absorption by Magnetic Materials*, edited by J. Chikawa, J. R. Helliwell, and S. W. Lovesey (Oxford University Press, New York, 1996), Oxford Series on Synchrotron Radiation, Vol. 1.

[66] H. Kimura, T. Hirono, Y. Tamenori, Y. Saitoh, N. Salashchenko, and T. Ishikawa, Journal of Electron Spectroscopy and Related Phenomena **144-147**, 1079 (2005).

[67] T. Hirono, H. Kimura, T. Muro, Y. Saitoh, and T. Ishikawa, Journal of Electron Spectroscopy and Related Phenomena **144-147**, 1097 (2005).

[68] X.-L. Qi and S.-C. Zhang, Reviews of Modern Physics **83**, 1057 (2011).

[69] J. E. Moore, Nature **464**, 194 (2010).

[70] M. Z. Hasan and C. L. Kane, Reviews of Modern Physics **82**, 3045 (2010).

[71] Y. Sakamoto, T. Hirahara, H. Miyazaki, S.-i. Kimura, and S. Hasegawa, Physical Review B **81**, 165432 (2010).

[72] Y. Zhang, K. He, C.-Z. Chang, C.-L. Song, L.-L. Wang, X. Chen, J.-F. Jia, Z. Fang, X. Dai, W.-Y. Shan, et al., Nature Physics **6**, 584 (2010).

[73] M. S. Bahramy, P. D. C. King, A. de la Torre, J. Chang, M. Shi, L. Patthey, G. Balakrishnan, P. Hofmann, R. Arita, N. Nagaosa, et al., Nature Communications **3**, 1159 (2012).

[74] G. Landolt, S. Schreyeck, S. V. Eremeev, B. Slomski, S. Muff, J. Osterwalder, E. V. Chulkov, C. Gould, G. Karczewski, K. Brunner, et al., Physical Review Letters **112**, 057601 (2014).

[75] Y. L. Chen, J.-H. Chu, J. G. Analytis, Z. K. Liu, K. Igarashi, H.-H. Kuo, X. L. Qi, S. K. Mo, R. G. Moore, D. H. Lu, et al., Science **329**, 659 (2010).

[76] K. Nomura and N. Nagaosa, Physical Review Letters **106**, 166802 (2011).

[77] C.-Z. Chang, J. Zhang, X. Feng, J. Shen, Z. Zhang, M. Guo, K. Li, Y. Ou, P. Wei, L.-L. Wang, et al., Science **340**, 167 (2013).

[78] X. Kou, S.-T. Guo, Y. Fan, L. Pan, M. Lang, Y. Jiang, Q. Shao, T. Nie, K. Murata, J. Tang, et al., Physical Review Letters **113**, 137201 (2014).

[79] X.-L. Qi, T. L. Hughes, and S.-C. Zhang, Physical Review B **78**, 195424 (2008).

[80] X.-L. Qi, R. Li, J. Zang, and S.-C. Zhang, Science **323**, 1184 (2009).

[81] Y. S. Hor, P. Roushan, H. Beidenkopf, J. Seo, D. Qu, J. G. Checkelsky, L. A. Wray, D. Hsieh, Y. Xia, S.-Y. Xu, et al., Physical Review B **81**, 195203 (2010).

[82] J. G. Checkelsky, J. Ye, Y. Onose, Y. Iwasa, and Y. Tokura, Nature Physics **8**, 729 (2012).

[83] T. Goto, M. C. Onbasli, and C. A. Ross, Optics Express **20**, 28507 (2012).

[84] M. C. Onbasli, A. Kehlberger, D. H. Kim, G. Jakob, M. Kläui, A. V. Chumak, B. Hillebrands, and C. A. Ross, APL Materials **2**, 106102 (2014).

[85] S. A. Manuilov, R. Fors, S. I. Khartsev, and A. M. Grishin, Journal of Applied Physics **105**, 033917 (2009).

[86] S. Chikazumi and C. D. Graham, *Physics of Ferromagnetism, 2nd edition* (Clarendon Press, Oxford, 1997), p. 332.

[87] Y. Gotoh and S. Ino, Thin Solid Films **109**, 255 (1983).

[88] M. Neupane, A. Richardella, J. Sánchez-Barriga, S. Xu, N. Alidoust, I. Belopolski, C. Liu, G. Bian, D. Zhang, D. Marchenko, et al., Nature Communications **5**, 3841 (2014).

[89] S. Y. F. Zhao, C. Beekman, L. J. Sandilands, J. E. J. Bashucky, D. Kwok, N. Lee, A. D. LaForge, S. W. Cheong, and K. S. Burch, Applied Physics Letters **98**, 141911 (2011).

[90] P. S. Miedema and F. M. de Groot, Journal of Electron Spectroscopy and Related Phenomena **187**, 32 (2013).

[91] W. Noun, E. Popova, F. Bardelli, Y. Dumont, R. Bertacco, A. Tagliaferri, M. Tessier, M. Guyot, B. Berini, and N. Keller, Physical Review B **81**, 1 (2010).

[92] D. Song, L. Ma, S. Zhou, and J. Zhu, Applied Physics Letters **107**, 042401 (2015).

[93] M. Li, W. Cui, J. Yu, Z. Dai, Z. Wang, F. Katmis, W. Guo, and J. Moodera, Physical Review B **91**, 014427 (2015).

[94] Z. Q. Qiu and S. D. Bader, Review of Scientific Instruments **71**, 1243 (2000).

[95] D.-E. Jeong, K.-S. Lee, and S.-K. Kim, Applied Physics Letters **88**, 181109 (2006).

[96] D.-E. Jeong and S.-K. Kim, Physical Review B **78**, 012412 (2008).

[97] D.-E. Jeong and S.-K. Kim, Journal of Applied Physics **105**, 07E709 (2009).

[98] M. Taguchi, L. Braicovich, F. Borgatti, G. Ghiringhelli, A. Tagliaferri, N. B. Brookes, T. Uozumi, and A. Kotani, Physical Review B **63**, 245114 (2001).

[99] M. Taguchi, J. C. Parlebas, T. Uozumi, A. Kotani, and C.-C. Kao, Physical Review B **61**, 2553 (2000).

[100] M. Taguchi and G. van der Laan, Physical Review B **66**, 140401 (2002).

[101] L. Henke, E. Gullikson, and J. C. Davis, URL `http://henke.lbl.gov/optical_constants/getdb2.html`.

[102] R. Cowan, *Theory of Atomic Structure and Spectra* (University of California Press, Berkeley, 1981).

[103] K. Fukui, H. Ogasawara, A. Kotani, T. Iwazumi, H. Shoji, and T. Nakamura, Journal of the Physical Society of Japan **70**, 3457 (2001).

[104] H. Ebert, a manual of the SPR-KKR code, URL `http://olymp.cup.uni-muenchen.de/index.php?option=com_remository&Itemid=20&func=startdown&id=51&lang=en`.

[105] J. Minár and H. Ebert, Surface Review and Letters **9**, 1179 (2002).

[106] J. Minár and H. Ebert, Journal of Applied Physics **91**, 7349 (2002).

[107] C.-Y. You and S.-C. Shin, Applied Physics Letters **69**, 1315 (1996).

[108] Y. Saitoh, H. Kimura, Y. Suzuki, T. Nakatani, T. Matsushita, T. Muro, T. Miyahara, M. Fujisawa, K. Soda, S. Ueda, et al., Review of Scientific Instruments **71**, 3254 (2000).

[109] T. Hara, T. Tanaka, T. Tanabe, X.-M. Marechal, K. Kumagai, and H. Kitamura, Journal of Synchrotron Radiation **5**, 426 (1998).

[110] T. Hara, K. Shirasawa, M. Takeuchi, T. Seike, Y. Saito, T. Muro, and H. Kitamura, Nuclear Instruments and Methods in Physics Research Section A: Accelerators, Spectrometers, Detectors and Associated Equipment **498**, 496 (2003).

[111] T. Muro, T. Nakamura, T. Matsushita, T. Wakita, K. Fukumoto, H. Kimura, T. Hirono, T. Kinoshita, T. Hara, K. Shirasawa, et al., AIP Conference Proceedings **879**, 571 (2007).

[112] Y. Saitoh, Y. Fukuda, Y. Takeda, H. Yamagami, S. Takahashi, Y. Asano, T. Hara, K. Shirasawa, M. Takeuchi, T. Tanaka, et al., Journal of Synchrotron Radiation **19**, 388 (2012).

[113] T. Nakamura and M. Suzuki, Journal of the Physical Society of Japan **82**, 021006 (2013).

[114] A. Rogalev, F. Wilhelm, N. Jaouen, J. Goulon, and J.-P. Kappler, in *Magnetism: A Synchrotron Radiation Approach*, edited by E. Beaurepaire, H. Bulou, F. Scheurer, and J.-P. Kappler (Springer, Berlin, 2006), Lecture Notes in Physics, Vol. 697, p. 84.

[115] F. Wilhelm, P. Poulopoulos, H. Wende, A. Scherz, K. Baberschke, M. Angelakeris, N. K. Flevaris, and A. Rogalev, Physical Review Letters **87**, 207202 (2001).

[116] M. Suzuki, H. Muraoka, Y. Inaba, H. Miyagawa, N. Kawamura, T. Shimatsu, H. Maruyama, N. Ishimatsu, Y. Isohama, and Y. Sonobe, Physical Review B **72**, 054430 (2005).

[117] J. K. Furdyna, Journal of Applied Physics **64**, R29 (1988).

[118] M. Ye, W. Li, S. Zhu, Y. Takeda, Y. Saitoh, J. Wang, H. Pan, M. Nurmamat, K. Sumida, F. Ji, et al., Nature Communications **6**, 8913 (2015).

[119] S. Imada, A. Yamasaki, S. Suga, T. Shima, and K. Takanashi, Applied Physics Letters **90**, 132507 (2007).

[120] C. J. Sun, G. M. Chow, G. H. Fecher, J. S. Chen, H.-J. Lin, and Y. Hwu, Japanese Journal of Applied Physics **45**, 2539 (2006).

[121] M. M. Soares, H. C. N. Tolentino, M. De Santis, A. Y. Ramos, and J. C. Cezar, Journal of Applied Physics **109**, 07D725 (2011).

[122] C.-H. Lambert, S. Mangin, B. S. D. Ch. S. Varaprasad, Y. K. Takahashi, M. Hehn, M. Cinchetti, G. Malinowski, K. Hono, Y. Fainman, M. Aeschlimann, et al., Science **345**, 1337 (2014).

[123] J. Zhang, C.-Z. Chang, Z. Zhang, J. Wen, X. Feng, K. Li, M. Liu, K. He, L. Wang, X. Chen, et al., Nature Communications **2**, 574 (2011).

[124] M. Suzuki, N. Kawamura, M. Mizumaki, A. Urata, H. Maruyama, S. Goto, and T. Ishikawa, Japanese Journal of Applied Physics **37**, L1488 (1998).

[125] I. Matsuda, A. Kuroda, J. Miyawaki, Y. Kosegawa, S. Yamamoto, T. Seike, T. Bizen, Y. Harada, T. Tanaka, and H. Kitamura, Nuclear Instruments and Methods in Physics Research Section A: Accelerators, Spectrometers, Detectors and Associated Equipment **767**, 296 (2014).

[126] H. A. Algra and P. Hansen, Applied Physics A Solids and Surfaces **29**, 83 (1982).

[127] L. L. Landau and E. M. Lifshitz, *Electrodynamics of Continuous Media* (Pergamon Press, 1960).

[128] H.-C. Mertins, O. Zaharko, A. Gaupp, F. Schäfers, D. Abramsohn, and H. Grimmer, Journal of Magnetism and Magnetic Materials **240**, 451 (2002).

[129] J. P. van der Ziel, P. S. Pershan, and L. D. Malmstrom, Physical Review Letters **15**, 190 (1965).

[130] A. Kirilyuk, A. V. Kimel, and T. Rasing, Reviews of Modern Physics **82**, 2731 (2010).